Geochemistry, Geophysics, Geosystems

RESEARCH ARTICLE
10.1029/2023GC011353

Key Points:
- The 20 February 2023 *Mw* 6.4 Hatay (Türkiye) earthquake indicates a normal fault mechanism with a significant left-lateral strike-slip component
- Transtensional deformation is evident in the Hatay-Syria (SE Türkiye) region
- Most of the 2023 Hatay-Syria aftershocks appear to concentrate on the depth range of 10–20 km of the crust

Supporting Information:

Supporting Information may be found in the online version of this article.

Correspondence to:

S. Yolsal-Çevikbilen,
yolsalse@itu.edu.tr

Citation:

Yolsal-Çevikbilen, S., Taymaz, T., Irmak, T. S., Erman, C., Kahraman, M., Özkan, B., et al. (2024). Source geometry and rupture characteristics of the 20 February 2023 Mw 6.4 Hatay (Türkiye) earthquake at southwest edge of the East Anatolian Fault. *Geochemistry, Geophysics, Geosystems*, *25*, e2023GC011353. https://doi.org/10.1029/2023GC011353

Received 13 NOV 2023
Accepted 28 SEP 2024

Source Geometry and Rupture Characteristics of the 20 February 2023 Mw 6.4 Hatay (Türkiye) Earthquake at Southwest Edge of the East Anatolian Fault

Seda Yolsal-Çevikbilen[1], Tuncay Taymaz[1], Tahir Serkan Irmak[2], Ceyhun Erman[1], Metin Kahraman[3], Berkan Özkan[1], Tuna Eken[1], Taylan Öcalan[4], Ali Hasan Doğan[4,5], and Cemali Altuntaş[4]

[1]Department of Geophysical Engineering, The Faculty of Mines, İstanbul Technical University (ITU), İstanbul, Türkiye, [2]Department of Geophysical Engineering, Kocaeli University, Kocaeli, Türkiye, [3]Eurasia Institute of Earth Sciences, İstanbul Technical University, İstanbul, Türkiye, [4]Department of Geomatic Engineering, Yıldız Technical University, İstanbul, Türkiye, [5]Department of Geomatics Engineering, Gaziosmanpaşa University, Tokat, Türkiye

Abstract Following the catastrophic 6 February 2023 *Mw* 7.8 and *Mw* 7.6 Kahramanmaraş earthquakes in the East Anatolian Fault Zone (EAFZ; southeast Türkiye), numerous aftershocks occurred along the major branches of this left-lateral shear zone. The spatio-temporal distribution of the earthquakes implied the stress-triggering effects of co-seismic ruptures on closely connected fault segments over large distances. On the 20 February 2023 two earthquakes with *Mw* 6.4 and *Mw* 5.2 struck Hatay (Türkiye) located near the Samandağ-Antakya segment of the EAFZ. To understand the rupture evolution of these earthquakes, we first re-located the aftershock sequence that occurred over a 3-month period in the Hatay-Syria region. A normal faulting mechanism with a significant amount of left-lateral strike-slip component at a shallow focal depth of 12 km was estimated for the 2023 *Mw* 6.4 earthquake from the inversion of seismological data. Our slip models describe a relatively simple and unilateral rupture propagation along about 36 km-long active segments of the EAFZ. The co-seismic horizontal displacements inferred from the Global Navigation Satellite System data are compatible with the oblique slip kinematics. Furthermore, we suggest that this earthquake did not produce notable tsunami waves on the adjacent coasts since the rupture plane did not extend to the seafloor of the Eastern Mediterranean with substantial amount of vertical displacement. We reckon that a future large earthquake (Mw ≥ 7.0) in the Hatay-Syria region where increased stress was transferred to the fault segments of the EAFZ and the Dead Sea Fault Zone (DSFZ) after the 2023 earthquakes will be a probable source of tsunami at the coastal plains of the Eastern Mediterranean Sea region.

Plain Language Summary The destructive 6 February 2023 *Mw* 7.8 and *Mw* 7.6 SE Türkiye earthquakes triggered an intense seismic activity along the major segments of the East Anatolian Fault Zone (EAFZ) in SE Türkiye. On 20 February 2023, distinct earthquake clusters occurred along the Amanos and Samandağ-Antakya segments in the southwest edge of the EAFZ. In this manuscript, source characteristics and rupture kinematics of the 20 February 2023 *Mw* 6.4 Hatay (Türkiye) earthquake were estimated by analyzing seismological and geodetic data. Our results mainly indicate a normal faulting mechanism with a significant amount of left-lateral strike-slip component for this earthquake. The slip models show a simple slip distribution pattern along the strike of the fault plane that lasted about 10–12 s. The analyzed time series of the available Global Navigation Satellite System stations present horizontal co-seismic displacements consistent with oblique slip kinematics of the rupture. We finally suggest that this earthquake serves as a reminder of the seismic and tsunami hazard potential in the Hatay-Syria area.

1. Introduction

In February 2023, intense seismicity including catastrophic earthquakes (Mw ≥ 7.5) occurred along the major segments of the left-lateral strike-slip EAFZ in SE Türkiye, which forms a part of the collisional boundary between the Arabian and the Anatolian plates. The 6 February 2023 *Mw* 7.8 Nurdağı-Pazarcık and *Mw* 7.6 Ekinözü-Elbistan (Kahramanmaraş) earthquakes that are the largest seismic events that have occurred in Türkiye since 1939 are located on the Pazarcık and Sürgü-Çardak segments of the EAFZ, respectively. They initiated numerous aftershock sequences, and produced large-scale surface ruptures with significant amount of horizontal displacements up to 8–10 m on the faulting area (Goldberg, Taymaz, Reitman, et al., 2023; Goldberg, Taymaz, Yeck,

10.1029/2023GC011353

et al., 2023; Li et al., 2023; Liu et al., 2023; Mai et al., 2023; Melgar et al., 2023; Okuwaki et al., 2023; USGS, 2023a, 2023b; Z. Wang et al., 2023; Wu et al., 2023; C. Xu et al., 2023; Zahradnik et al., 2023; Zhang et al., 2023). The horizontal ground accelerations were recorded to be locally up to 2 g during the *Mw* 7.8 Nurdağı-Pazarcık earthquake, and it caused severe and widespread shaking in the Hatay-Antakya area with values of about 0.5 g with evident mapped cracks and surface ruptures before the 2023 *Mw* 6.4 earthquake (Mai et al., 2023).

Two weeks later, on the 20 February 2023 (OT: 17:04:27 and OT: 17:07:33 UTC), moderate-to-large earthquakes with *Mw* 6.4 and *Mw* 5.5 hit the Defne, Yayladağı and Samandağ (Hatay, southern Türkiye) provinces at the southwestern end of the EAFZ (AFAD, 2023a, 2023b; KOERI, 2023a, 2023b; MTA, 2023; USGS, 2023c, 2023d; Figure 1 and Table 1). These earthquakes were strongly felt in several cities in the south-eastern and south-central Anatolia by causing severe damage and destruction with causalities near the epicentral area. The occurrence of both earthquakes within a remarkably brief timeframe, accompanied by nearly identical source mechanisms, has attracted great interest, in particular, due to their potential to yield valuable insights into the most recent types of deformation and triggering effects observed within the closely interconnected segments of the EAFZ. This type of earthquake occurrence has been recently observed along the North Anatolian Fault Zone, the EAFZ, and other well-known strike-slip faults in the Eastern Mediterranean Sea region, such as the 2020 Yedisu-Karlıova and the 2020 Qotur-Ravian earthquake doublets (e.g., Taymaz, Ganas, et al., 2022). Fast and automatic focal mechanism solutions of the 20 February 2023 *Mw* 6.4 and *Mw* 5.5 earthquakes were reported by several national and international seismological institutes (Table S1 in Supporting Information S1). However, there is a slight confusion about the existence and magnitude of the second largest earthquake on the 20 February 2023. While USGS (2023c) and AFAD (2023a) reported a magnitude of 5.5 for this earthquake (OT: 17:07:33 UTC), KOERI (2023a) released an earthquake magnitude of 4.5 at the same time and location. The others (e.g., GFZ, INGV, GCMT as such) did not provide any information about this event. The reported solutions clearly indicated normal faulting mechanisms with significant left-lateral strike slip components at shallow focal depths for both events as compatible with the active tectonic structures in the study region. The epicenters of the earthquakes are very close to the intersection area of the EAFZ, the DSFZ and Cyprus arc where the significant stress increases were transferred to the segments of these faults after the 6 February 2023 earthquakes (Dai et al., 2024; Liu et al., 2023; Melgar et al., 2023; Stein et al., 2023; Toda et al., 2023). Furthermore, these provinces hosted several large and strong historical earthquakes ($M_w \geq 7.0$) that produced damaging tsunami waves along the eastern Mediterranean coastal plains (Table 2). Following the *Mw* 7.8 and *Mw* 7.6 SE Türkiye earthquakes, ~15–20 cm sea level rise was recorded at four tide gauge stations, for example, İskenderun-Arsuz, Mersin-Erdemli, Gazimagusa and Girne (Cyprus) in the Eastern Mediterranean Sea region (Heidarzadeh et al., 2023; Hu et al., 2023; Medvedeva et al., 2023; METU-EERC, 2023). Therefore, a tsunami warning was given by the national seismological and tsunami centers of Türkiye to the adjacent coastal plains (e.g., İskenderun bay and Levantine basin) immediately after the 2023 *Mw* 6.4 earthquake. Tsunami amplitudes of about 0.2 and 0.5 m were initially estimated for the Hatay-Syria coastal plains (KOERI, 2023b). But the warning was withdrawn in a short time (about 2 hr) later due to the lack of evident observation for tsunami generation at the nearby Eastern Mediterranean coasts.

The study area is located on the south-eastern part of the Anatolian plate, adjacent to the collisional borders between the African, the Arabian, and Anatolian plates (Figure 1). Due to the interaction of these three major lithospheric plates, the active tectonics of SE Türkiye is highly complex with many large-scale geological structures such as the EAFZ, the DSFZ and the Cyprus arc. They are mainly responsible for the generation of destructive earthquakes in the region (e.g., Arpat & Şaroğlu, 1972; Bozkurt, 2001; Hempton et al., 1981; Jackson & McKenzie, 1984; Lyberis et al., 1992; Şengör et al., 1985; Taymaz et al., 1991; Taymaz, Ganas, et al., 2022; Taymaz, Yolsal-Çevikbilen, et al., 2022; Türkelli et al., 2003). The 580 km-long the EAFZ is a left-lateral strike-slip fault zone extending between Karliova in northeast and Antakya, which links to the DSFZ and the Cyprus Arc around the Amik Triple Junction (ATJ) in the southern Türkiye. It has several segments along its strike such as Sürgü-Çardak (SüF), Narli, Sakçagöz, Amanos (AS), Samandağ-Antakya (SAFZ), Yesemek (YS) and Karasu Valley Fault (KV). The 350 km-long major segment of EAFZ is associated to the fault partitioning toward the Sürgü-Çardak (SüF) and then it merges with Kozan-Misis fault system (KoFZ and KFZ) in the Gulf of Iskenderun (e.g., Duman & Emre, 2013; Emre et al., 2012, 2013, 2018; McKenzie, 1976; Şaroğlu et al., 1992a, 1992b; Tarı et al., 2014; Taymaz et al., 1991, 2021) (Figures 1 and 2).

Geodetic measurements reveal that the slip rate is approximately 15 ± 3 mm/yr along the EAFZ, 10.0 ± 0.3 mm/yr for the Palu—Hazar Lake segment and 9.9 ± 0.2 mm/yr for the Hazar Lake—Türkoglu segment of the EAFZ

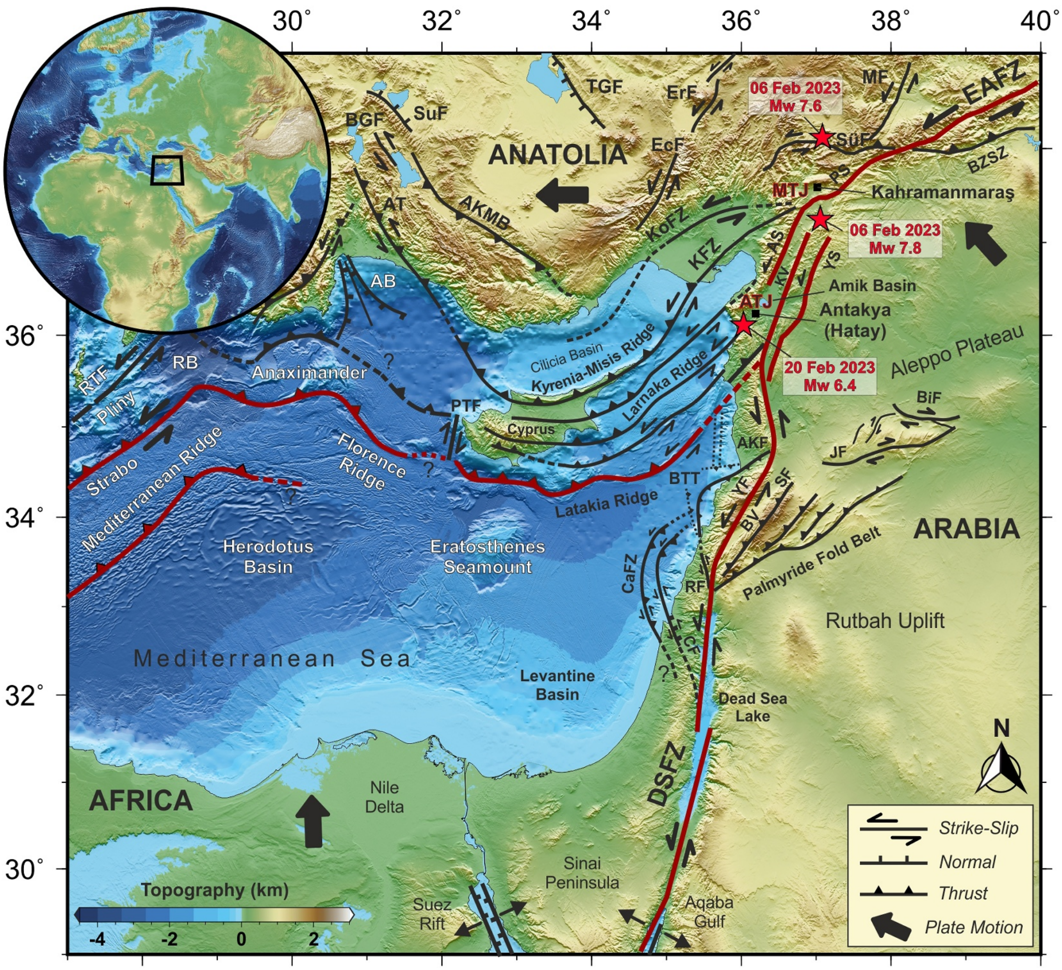

Figure 1. A sketch map of plate boundaries (thick red lines) and tectonic structures in the Eastern Mediterranean Sea and surroundings based on the studies of Garfunkel et al. (1981), Kempler and Garfunkel (1994), Salamon et al. (1996, 2003), McClusky et al. (2000), Woodside et al. (2002), Zanchi et al. (2002), Tan and Taymaz (2006), Gardosh and Druckman (2006), Schattner and Ben-Avraham (2007), Yolsal (2008), Ben-Avraham et al. (2008), Hall et al. (2008), Aksu et al. (2008), Yolsal-Çevikbilen & Taymaz (2012), Emre et al. (2012, 2013, 2018), Duman and Emre (2013), and Taymaz et al. (1991, 2021). The re-located epicenters of 6 February 2023 *Mw* 7.8 and *Mw* 7.6, and 20 February 2023 *Mw* 6.4 SE Türkiye earthquakes are shown with the red stars. 15 arc-sec topography data are taken from USGS/NASA SRTM15 + V2 (Tozer et al., 2019), and bathymetric compilations are after GEBCO_2020 Grid (https://www.gebco.net). The inset figure shows the location of the study area. *Abbreviations:* AB, Antalya Basin; AKF, Akkar Fault; AKMB, Aksu, Köprü, Manavgat Basin; AT, Aksu Thrust; ATJ, Amik Triple junction; AS, Amanos Segment; BiF, Bishri Fault; BGF, Beyşehir Gölü Fault; BTT, Beirut-Tripoli Thrust, BV, Bekaa Valley; BZSZ, Bitlis-Zagros Suture Zone; CaFZ, Carmel Fault Zone; CF, Carmel Fault; DSFZ, Dead Sea Fault Zone; EAFZ, East Anatolian Fault Zone; EcF, Ecemiş Fault; ErF, Erciyes Fault; JF, Jhar Fault; KFZ, Karataş Fault Zone; KoFZ, Kozan Fault Zone; KV, Karasu valley; MF, Malatya Fault; MTJ, Maraş Triple Junction; PS, Pazarcık Segment; PTF, Paphos Transform Fault; RB, Rhodes Basin; RF, Roum Fault; RTF, Rhodes Transform Fault; SF, Serghaya Fault; SuF, Sultandağları Fault; SüF, Sürgü-Çardak Fault; TGF, Tuz Gölü Fault; YF, Yammouneh Fault; YS, Yesemek Segment.

(Reilinger et al., 2006). In addition, Yıldız et al. (2020) estimated a left-lateral 4.4–5.4 mm/yr and a normal component slip rate of 3.0 mm/yr along the Karasu segment. They also emphasized the probability of a major earthquake with a magnitude of 6.8–7.2 along this fault. The earthquakes along this segment predominantly indicate normal faulting mechanism with large amount of left-lateral strike slip component at shallow focal depths, which are closely linked to the transtensional deformation between the strike-slip fault segments of the EAFZ and DSFZ (e.g., Salamon et al., 1996, 2003). Furthermore, Lattakia and Larnaka ridge segments of the Cyprus arc, dominated by a left-lateral shear zone, play a key role in developing complex deformation styles in the region and rupture kinematics of the earthquakes (Figures 1 and 2). Stress inversion studies primarily revealed

Table 1

Source Parameters of Earthquakes (Mw ≥ 4.9) That Have Occurred Along the Western Segments of the East Anatolian Fault Zone (EAFZ) at South-Central Türkiye and Along the Dead Sea Fault Zone (DSFZ)

Date (d.m.y)	Origin time (UTC, h:m:s)	Lat. (°N)	Lon. (°E)	Mw	h (km)	Nodal Plane-1 (ϕ°/δ°/λ°)	Nodal Plane-2 (ϕ°/δ°/λ°)	$M_o \times 10^{17}$ Nm	SV1 (°) (Az/Pl)	SV2 (°) (Az/Pl)	*P* (°) (Az/Pl)	*T* (°) (Az/Pl)	References
24.06.1989	03:09:58	36.28	36.13	5.1	15	203/28/−93	27/62/−88	0.504	296/28	113/62	300/73	115/17	GCMT
22.03.1993	11:03:43	34.70	34.38	5.3	35	169/43/64	23/52/112	0.974	113/38	259/47	97/5	352/72	Y08
22.01.1997	17:57:23	36.19	35.94	5.9	4	217/19/−16	322/85/−108	8.880	232/5	127/71	213/47	68/37	Ç02
26.03.1997	04:22:51	33.39	35.45	5.6	10	104/35/−167	4/83/−56	0.610	273/7	14/55	306/42	66/29	INGV
27.06.1998	13:55:53	36.85	35.33	6.1	20	51/77/17	317/73/166	29.20	47/17	141/13	184/2	275/21	T04
04.07.1998	02:15:51	36.63	35.42	5.4	15	338/84/145	72/55/8	1.590	162/35	68/6	30/19	289/29	GCMT
29.03.2006	22:05:18	35.41	35.41	5.0	19.6	317/83/−132	219/43/−10	0.343	129/48	227/7	190/37	79/26	GCMT
15.02.2008	10:36:21	33.27	35.32	5.1	12.1	336/78/−22	71/69/−167	0.656	341/21	246/12	292/24	25/6	GCMT
14.11.2010	23:08:26	36.58	36.02	4.9	10	203/34/−115	52/60/−74	0.340	322/30	113/56	359/71	131/13	INGV
11.05.2012	18:48:30	34.25	34.17	5.5	20	116/74/−1	206/89/−164	1.050	116/1	26/16	72/12	340/11	INGV
14.02.2014	00:33:39	36.23	36.07	4.9	18	155/36/−144	35/70/−59	0.251	305/20	65/54	343/55	102/19	GCMT
29.07.2015	22:00:55	36.56	34.97	4.9	34	21/53/−53	149/51/−128	0.323	60/40	291/37	353/61	86/1	USGS-RMT
15.04.2020	07:40:06	35.73	35.47	4.9	24.7	219/47/−10	316/83/−137	0.278	226/7	129/43	187/35	80/23	GCMT
10.06.2022	01:40:21	34.83	33.87	5.0	40.5	351/35/101	158/55/82	0.452	248/34	81/55	253/10	41/78	USGS-W Phase
16.02.2023	19:47:50	36.21	35.66	5.1	13	172/31/−99	3/58/−84	0.520	272/31	82/59	287/75	89/14	GFZ
20.02.2023	**17:04:27**	**36.10**	**36.04**	**6.4**	**12**	**208/30/−28**	**323/76/−117**	**51.78**	**233/14**	**118/60**	**202/51**	**74/27**	**This study**
20.02.2023	**17:07:33**	**36.21**	**35.93**	**5.2**	**12**	**244/50/−21**	**348/74/−138**	**0.73**	**258/16**	**154/40**	**214/40**	**111/15**	**This study**
23.02.2023	15:53:49	36.14	35.92	4.9	13	221/58/−73	10/35/−115	0.310	281/54	131/32	172/71	299/11	GFZ

Note. The bold values display those of the 20 February 2023 earthquakes obtained in this study. Mw: Moment Magnitude, M_o: Seismic Moment, h: Focal depth (km), ϕ: strike (°), δ: dip (°), λ: rake (°), SV: Slip Vector, Az/Pl: Azimuth/Plunge, *P*: *P*-axis, *T*: *T*-axis, Refs: ***References***, Ç02: Çalışkan (2002); T04: Tan (2004); Y08: Yolsal (2008), GCMT: Global Centroid Moment Tensor; USGS-RMT United States Geological Survey; INGV: Istituto Nazionale di Geofisica e Vulcanologia (Italy) (Figure 2).

extensional (with vertical $\sigma 1$) and left-lateral shear deformation patterns along the 145-km long NNE trending Amanos Segment (AS; Lyberis et al., 1992) and the continuation of Cyprus Arc and Narlı segment of the EAFZ, respectively (Güvercin et al., 2022; Över et al., 2002, 2023).

The ∼1,000 km long the left-lateral the DSFZ at south, which was another tectonic structure controlling the intense deformation in the study area, accommodates the relative motion between the African and the Arabian plates (Freund, 1965; Garfunkel et al., 1981; Hofstetter et al., 2007; Lyberis et al., 1992; Nur & Ben-Avraham, 1978; Zanchi et al., 2002). It extends in the about N-S direction between the Red Sea spreading center in the south and the northern boundary of the Arabian plate delineated by the EAFZ in SE Türkiye (Figure 1). In general, there is much more earthquake activity in the southern parts of the DSFZ (e.g., Gulf of Aqaba) compared to its northern branches. Source mechanisms of the earthquakes along the DSFZ denoted to left-lateral strike-slip faulting mechanisms with dip-slip components that are mostly associated with the en-echelon faults and asymmetrical folding structures in the region (e.g., Hofstetter et al., 2007; Salamon et al., 1996, 2003; Yolsal, 2008).

In this study, our main goal is to resolve the source and rupture characteristics of the 20 February 2023 *Mw* 6.4 earthquake and its major aftershock by analyzing the multi-scale seismological and geodetic data sets with routine inversion processes. To achieve this aim, we first relocated the 3-month long earthquake sequence to constrain the correlation between the aftershocks and the existing fault segments in the area. We obtained the rupture geometry and source parameters of these earthquakes by inverting teleseismic and regional-distance waveforms. In addition to these, Global Navigation Satellite System (GNSS) data was analyzed to quantify co-seismic displacements observed along the faulted area, in particular related to the 2023 *Mw* 6.4 Hatay earthquake. To emphasize the

10.1029/2023GC011353

Table 2
Large Historical Earthquakes Occurred Along the EAFZ and DSFZ and Surrounding Regions

Date (dd-mm-yyyy)	Lat (°N)	Lon (°E)	I_o or M_s	Location/Affected region	References
EAFZ, EAFZ + DSFZ combined, and the Cyprus arc					
BC-69	36.25	36.10	IX	Antakya, Syria	KOERI
37	36.00	36.30	VIII	Antakya, Dafneh	AJ98, S05
53	36.20	36.50	VIII	Antakya, Afamia, Lattakia	S05
13-12-115	35.80	36.30	X–XI	Antakya, Orontes River (Syria)	P80, AJ98
110	36.20	36.00	VIII	Antakya, Samandağ	E67
245	36.25	36.10	X	Antakya	KOERI
334	36.25	36.10	IX	Antakya, Beirut, Cyprus	KOERI
14-09-458	36.25	36.10	IX	Antakya, Samandağ (80.000 deaths)	P80, KOERI
10-09-506	36.25	36.10	IX	Antakya, Samandağ	KOERI
29-05-526	36.25	36.10	IX	Antakya, Samandağ	P80, KOERI
527-529	36.23	36.10	X	Antakya	E67, P80
587-588	36.25	36.10	IX	Antakya (60.000 deaths)	P80, KOERI
20-03-713	36.23	36.10	IX	Antakya	E67, P80
08-04-859	36.25	36.10	IX	Antakya	P80, KOERI
867	36.25	36.10	IX	Antakya	KOERI
10-08-1114	36.50	35.50	IX	Ceyhan, Antakya, Maraş (Tsunami)	KOERI
12/15-08-1157	35.00	36.50	7.8	Hama, Syria, Lebanon	AB89, AJ98, G04
29-07-1170	35.90	36.40	IX-X	Idlib, Aleppo (80.000 deaths)	P80, AB89
11/22-02-1404	35.90	36.30	IX	Hatab, Aleppo	P80, AB89, S05
1407–1408	35.66	36.17	IX-XI	Lattakia, Syria (Tsunami)	P80, AB89, AJ98, Y07
21-01-1626	36.50	37.10	IX	Aleppo, Gaziantep, Hama	S05
26-04-1796	35.50	36.00	6.6	Latakia (Syria)	AB89, AJ98, S05
13-08-1822	**36.70**	**36.90**	**7.4**	**Antakya (200 km faulting), Tsunami**	**P80, AB89, AJ98, S05, Y07**
02-04-1872	36.25	36.10	IX	Antakya, Samandağ (1800 deaths)	P80, KOERI
03-04-1872	36.40	36.50	7.2	Hatay, Halep, Beirut, İskenderun, Amik Gölü (20 km faulting and Tsunami)	A89, AB89, AJ98, S05, Y07
14-07-1936	36.50	36.00	VII	Near Antakya	E67, P80
20-01-1941	35.20	33.60	IX	Cyprus	E67
08-04-1951	36.60	36.30	VII	Near Antakya	E67, P80
Dead Sea Fault Zone (DSFZ) only					
303-304	33.80	34.30	7.1	Saida, Sur, Syria	S05
22-08-502	33.00	34.80	7.2	Akka, Sur, Saida, Beirut, Safad	S05
18-01-747	32.50	35.60	7.2	Mt. Tabor, Bosra, Damascus	S05
29-05-1068	32.56	35.28	IX	Ramia, Kudus	GC05, S00
20-05-1202	33.43	35.75	X	Syria-Lebanon	AB89, AJ98, S05, GC05
30-10-1759	33.10	35.60	VIII	Hatay, Gaza, Cyprus, Trablus	BM79, AB89, A89, S05, Y07
25-11-1759	33.70	35.90	7.4	Bekaa, Lattakia, Gaza, Beirut (Destruction and Tsunami)	BM79, AB89, AJ98, S05, Y07
01-01-1837	33.20	35.50	7.4	Bshara (Lebanon)	AJ98
16-03-1956	33.30	35.70	IX	Lebanon (138 deaths, 30.000 homeless)	E67

Note. The numerical tsunami simulations of the 13 August 1822 earthquake marked in bold discussed in the Supporting Information S1. I_o: Intensity, M_S: magnitude, E67: Ergin et al. (1967), BM79: Ben-Menahem (1979), P80: Poirier et al. (1980); AB89: Ambraseys and Barazangi (1989); A89: Ambraseys (1989); A94: Ambraseys et al. (1994); AJ98: Ambraseys and Jackson (1998), S00: Soloviev et al. (2000); G04: Guidoboni et al. (2004); S05: Sbeinati et al. (2005); GC05: Guidoboni and Comastri (2005); Y07: Yolsal et al. (2007); KOERI: KOERI-UDIM (2012).

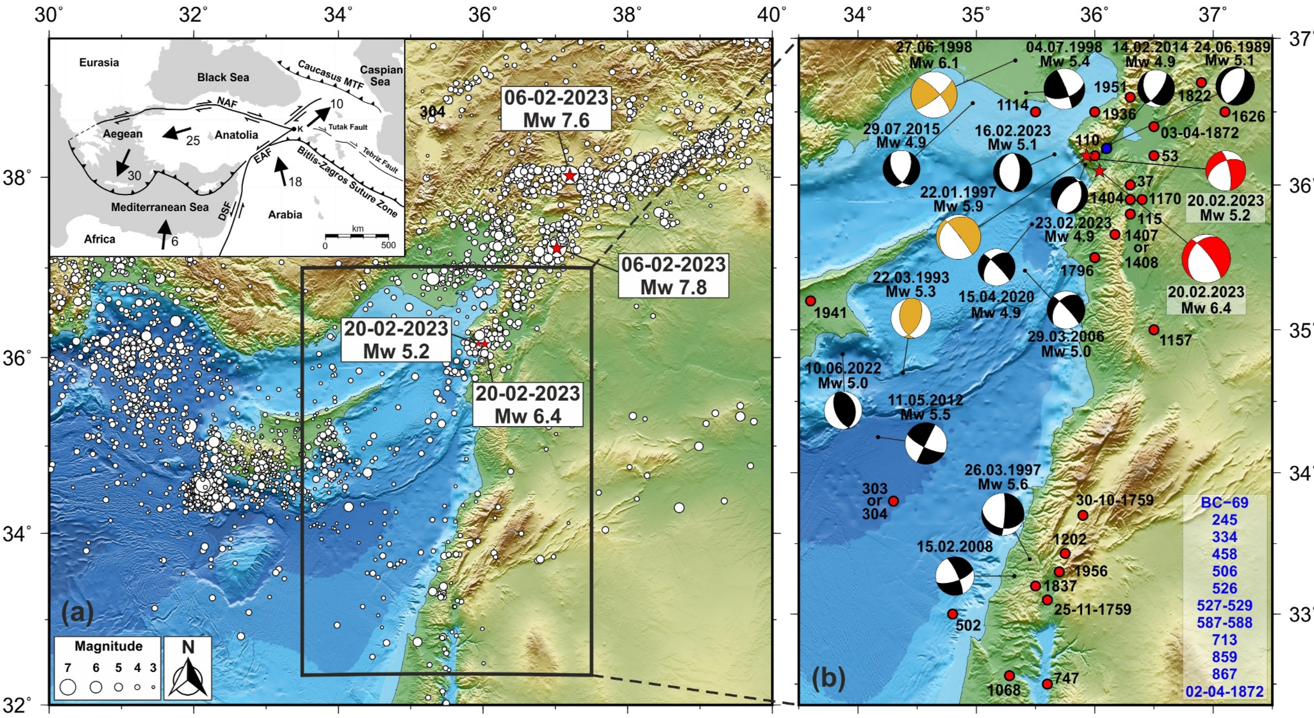

Figure 2. (a) Main tectonic structures and seismicity of the Eastern Mediterranean region (USGS-NEIC; 1973–2023; Mw ≥ 3.0). The relocated epicenters of 6 February 2023 Pazarcık and Ekinözü (Kahramanmaraş; *Mw* 7.8 and *Mw* 7.6) and 20 February 2023 Hatay (*Mw* 6.4 and *Mw* 5.2) earthquakes are shown with red stars, (b) Focal mechanism solutions of earthquakes (Mw ≥ 4.9) occurred along the EAFZ, east of Cyprus arc and DSFZ in the southernmost part of Türkiye. The red, yellow and black focal spheres indicate source mechanisms of earthquakes obtained by this study, other inversion-based studies (Çalışkan, 2002; Tan, 2004; Yolsal, 2008) and international seismological institutes (e.g., INGV, GCMT, USGS, GFZ; see Table 1), respectively. Historical earthquakes are also presented with red circles (see Table 2 for details). The dates of historical events concentrated at a one location, shown by a blue circle, are written on the lower-right side of the figure (b). *For the inset figure*, NAF, North Anatolian Fault; EAF, East Anatolian Fault; DSF, Dead Sea Fault. The GPS slip rates in mm/yr by the black arrows are taken from McClusky et al. (2000).

potential tsunami risk along the coastal plains of the Eastern Mediterranean near the 2023 *Mw* 6.4 epicentral area, we presented some of the results from the tsunami simulation of the historical 13 August 1822 Hatay-Syria tsunamigenic earthquake (Mw > 7.0–7.5) earlier performed by Yolsal (2008) and Yolsal-Çevikbilen & Taymaz (2012) in Supporting Information S1.

1.1. Recent and Historical Seismicity

The crustal and lithospheric structures beneath the EAFZ, the DSFZ and seismicity, source mechanisms and kinematic slip models of the earthquakes along these fault systems have been examined by numerous esteemed geological and seismological studies (e.g., Akyüz et al., 2006; Ambraseys & Barazangi, 1989; Dewey et al., 1986; Hubert-Ferrari et al., 2020; Khair et al., 2000; Melgar et al., 2020, 2023; Okuwaki et al., 2023; Ragon et al., 2021; Taymaz et al., 1991, 2021; Toda et al., 2023; H. Wang et al., 2020; Zor et al., 2003). In Hatay-Syria region, large and moderate-size (Mw ≥ 5.0) earthquakes mainly occur along the major segments of the EAFZ and the DSFZ (e.g., Samandağ-Antakya, Amanos, Yesemek, Sakçagöz and Narli segments, Amik Basin, Karasu Valley; Figures 1 and 2). Generally, they are characterized by shallow seismic activity in the 15–25 km of the upper crust, which associates to normal and/or left-lateral strike-slip faulting mechanisms with substantial dip-slip components (e.g., Çalışkan, 2002). The majority of earthquakes presented oblique normal faulting mechanisms that are presumably developed in response to nearly E-W, NE-SW and NW-SE extensional tectonic forces in the Amik Basin and the Karasu Valley area (e.g., Hofstetter et al., 2007; Salamon et al., 2003; Taymaz et al., 1991, 2021; Över et al., 2002, 2023). It is observed that the 20 February 2023 *Mw* 6.4 Hatay earthquake ruptured the NE-SW trending Samandağ-Antakya segment (SAFZ) of the EAFZ with numerous aftershocks located just close to the ATJ area that connects the EAFZ and the DSFZ to the Cyprus Arc in southern Türkiye (Table 1 and Figure 2).

In connection with the 2023 *Mw* 7.8 and *Mw* 7.6 SE Türkiye earthquakes, very frequent aftershock activity occurred along the major segments of the EAFZ and the DSFZ in Hatay-Syria region as documented by several studies (e.g., Ding et al., 2023; Inbal et al., 2023; Karabulut et al., 2023; Liu et al., 2023; Melgar et al., 2023; Petersen et al., 2023; Z. Wang et al., 2023) and many national and international agencies (e.g., USGS, GFZ, AFAD, GCMT, OCA, KOERI as such). The 20 February 2023 *Mw* 6.4 earthquake can be called as one of the largest aftershocks of these catastrophic events. On 16 February 2023, four days before the 2023 *Mw* 6.4 earthquake, a moderate-sized earthquake (*Mw* 5.1) occurred along the SAFZ. GFZ (2023) reported an obvious normal faulting mechanism for this event (strike: 172°; dip: 31°, rake: −99°, focal depth: 13 km; Table 1 and Figure 2). Similarly, OCA (2023) implied an oblique fault mechanism with strike of 29°, dip of 55° and rake angle of −25° at a 9-km focal depth for this earthquake. After the 20 February 2023 *Mw* 6.4 earthquake in Samandağ-Hatay province, another moderate-size event with *Mw* 5.5 occurred on the same day (OT: 17:07:33 UTC), and we examined its faulting geometry in this study. For this earthquake, USGS (2023d) reported a body-wave magnitude of *mb* 5.5 and an epicenter location of Latitude: 36.159°N and Longitude: 35.935°E. Additionally, AFAD (2023a) shared a moment tensor solution that suggests a normal faulting mechanism at a 25-km depth with a moment magnitude (*Mw*) of 5.5 (Table 1 and Table S1 in Supporting Information S1). Since we estimated a *Mw* of 5.2 for this earthquake by performing Regional Moment Tensor (RMT) inversion, we called this event the *Mw* 5.2 aftershock hereafter throughout the text.

Historical documents and catalogs emphasized several significant earthquakes with an intensity value of I_o = IX–X occurred in the Antakya-Hatay and Syria provinces in the eastern Mediterranean region in the past (e.g., Ambraseys, 1989; Ambraseys & Barazangi, 1989; Ambraseys & Jackson, 1998; Ambraseys & Melville, 1995; Ambraseys et al., 1994; Amiran et al., 1994; Ben-Menahem, 1979; Ergin et al., 1967; Guidoboni & Comastri, 2005; Guidoboni et al., 2004; Plassard & Kogoj, 1981; Poirier et al., 1980; Sbeinati et al., 2005; Soloviev et al., 2000; Yolsal et al., 2007; Yolsal-Çevikbilen & Taymaz, 2012). Ambraseys and Barazangi (1989) suggested a recurrence interval of destructive earthquakes in the Karasu Valley (KV) region as about 450-700 years. From palaeoseismological trench studies and field observations, Akyüz et al. (2006) defined three historical earthquakes (e.g., 859, 1408, and 1872) along the northern branch of the DSFZ near the ∼30 km-wide Amik Basin (AmB; Lyberis et al., 1992), and the probable recurrence interval for a large earthquake was suggested to be 506 ± 42 years along this segment of the fault. The earthquake epicenters in the Beqaa region are generally concentrated on the Yammouneh Fault (YF) in Lebanon, and the recurrence interval of large earthquakes for this region was obtained to be approximately 550–650 years (Khair et al., 2000). The source parameters of earthquakes (Mw ≥ 4.9) reported by prior studies are summarized in Table 1, while destructive historical earthquakes and associated tsunamis that largely affected the Antakya, Hatay, Syria and Levantine areas are listed in Table 2. We classified the source faults of these historical earthquakes as EAFZ, Cyprus arc, EAFZ + DSFZ and DSFZ only (Table 2), based primarily on their locations reported in the above-mentioned reliable catalogs/documents, and also on previous studies based on paleo- and archaeo-seismological analyses (e.g., Akyüz et al., 2006; Carena et al., 2023; Duman et al., 2020).

Among these historical earthquakes, the 13 August 1822 M_s 7.4 Hatay-Syria earthquake is one of the large and devastating events that occurred along the segments of the EAFZ and the DSFZ (Table 2). We noticed that the fault geometry assumed by Yolsal et al. (2007) and Yolsal (2008) for this historical earthquake is rather compatible with that of recent earthquakes that occurred along the SAFZ and Amanos Segment (AS) of the EAFZ (Figure S1 in Supporting Information S1). They numerically simulated the 1822 earthquake and its tsunami, and obtained large amplitude tsunami waves within 10–30 min in the Iskenderun Gulf, Levantine coasts and eastern part of the Cyprus Island, where destructive tsunami waves were also documented by historical records. Maximum positive tsunami amplitudes of ∼2–3 m along the Antakya-Hatay, Syria (tide gauges # 1, 2, 3, 11) and ∼2.5 m along the Adana coastal plains (#4, 5, 6, 7) were reported by these studies. In addition, they suggested ∼1.0–1.3 m tsunami waves arrived on Cyprus Island (tide gauges #8, 9, 10) in about 15 min, and ∼1.25 m at Gaza (Israel) coasts in ∼70 min (#12; Figure S1 in Supporting Information S1). However, any large amplitude tsunami waves were not estimated along the other Eastern Mediterranean coasts such as SW Anatolia, the Nile Delta and African coastal plains due to the dissipation of wave energy related to the long propagation distances, and the significant effects of natural bathymetrical barriers such as Cyprus Island and Eratosthenes Sea Mountains in the sea-bottom of the Eastern Mediterranean Sea (Figure S1 in Supporting Information S1). The other details about the tsunami simulation results can be found in Supporting Information S1.

2. Data

We analyzed seismological and HR-GNSS geodetic data using conventional methods to resolve the details of faulting geometry, rupture characteristics and kinematic finite-fault slip models of the 2023 Hatay (*Mw* 6.4 and *Mw* 5.2) earthquakes. We initially downloaded teleseismic (between 30° and 90°) long-period and broadband *P*- and *SH*- waveforms of the earthquake, recorded by seismic stations of FDSN-GDSN networks of the Data Management Center of the Incorporated Research Institutions for Seismology (IRIS-DMC) for point-source *P*- and *SH*-waveforms and kinematic finite-fault slip inversions (see Figures S2, S3, Tables S2, S3, and S4 in Supporting Information S1). We also retrieved strong ground-motion data and broadband three-component waveforms recorded at regional distance stations ($1° \leq \Delta \leq 10°$) from the national seismological institutions (e.g., AFAD and KOERI) for RMT inverse modeling and joint slip inversion (Figure S3, Tables S4, and S5 in Supporting Information S1). The selected stations for RMT analysis have the complete body and surface waveforms with good S/N ratios. To relocate the 2023 SE Türkiye earthquakes, including the 20 February 2023 *Mw* 6.4 and *Mw* 5.2 Samandağ - Hatay earthquakes and other aftershocks that occurred between the time period of 6 February 2023 and 8 May 2023, we further acquired the phase data from the Disaster and Emergency Management Presidency of Türkiye (AFAD). This includes *P*- and *S*- arrivals from available stations selected by an automatized earthquake detection based on the LTA/STA algorithm (Figure S4 and Table S6 in Supporting Information S1). The first 11 days of relocated aftershocks belonging to the 6 February 2023 SE Türkiye earthquakes were already published by Melgar et al. (2023). In addition, dual frequency high-rate GNSS observations of 11 stations from four different networks were analyzed (see Table S7 in Supporting Information S1; CORS-TR, ASKI, ELYA and TUDES) to obtain position time series for the 20 February 2023 *Mw* 6.4 Hatay earthquake occurred at OT: 17:04:27 (UTC). The distances between the GNSS stations and the earthquake epicenter span a range of ∼12–∼156 km. Data from 3 days before and 3 days after the earthquake were used to calculate displacements. In the processing step, the sampling interval was chosen as 30s and the positions were obtained in the ITRF2020 datum using an elevation mask of 7.5°. Then, the coordinates and their variance covariance matrices were transformed into topocentric coordinate system. In order to calculate horizontal and vertical displacements and their formal errors, the average values of the 3 days of data before and after the earthquake were calculated for each station.

3. Methods

In this section, we briefly summarized the seismological and geodetic approaches we employed and the relevant procedures in detail.

3.1. Earthquake Relocation Process

We relocated a total of 777 earthquakes, moment magnitudes ranging from 2.5 to 6.4, that occurred along the EAFZ in SE Türkiye for the duration of the three months after the 6 February 2023 *Mw* 7.8 and *Mw* 7.6 catastrophic Kahramanmaraş earthquakes. The analyzed data includes phase information from weak and strong ground-motion station networks. Initial absolute event locations were estimated by the *HypoInverse* algorithm (Klein, 2014). The majority of initial event locations focused on a depth range varying from 6.9 to 7.1 km. This almost constant depth distribution reflects a poor depth resolution for the aftershocks in such a complex fault regime. We performed *hypoDD* (Waldhauser & Ellsworth, 2000), a relative earthquake location algorithm, in order to calculate the more precise depth locations. The *hypoDD* uses the relative hypocenter locations and origin times for all observed event-station pairs, and then iteratively minimizes the difference between observed and calculated travel time residuals. It overcomes the potential bias caused by insufficient knowledge of structural complexities and velocity heterogeneities along the source-receiver path, and enables more robust and reliable hypocenter locations compared to traditional earthquake location algorithms (Waldhauser & Ellsworth, 2000). We created event pairs with inter-event distances of less than 10 km and with a minimum of 8 links to define up to 10 neighbors at all available stations located within 200 km distance from the center of the cluster. Relative locations and origin times were obtained from a single set of 15 iterations in which large residuals were underestimated to suppress potential bias on the solution. The initial 1D velocity model in *hypoDD* calculation was taken from Melgar et al. (2020) and Taymaz et al. (2021). The velocity model was modified using the 24 January 2020 *Mw* 6.7 Doğanyol–Sivrice earthquake and its aftershock sequences by inverting and updating phase arrivals (Kissling et al., 1994). As a result of the *hypoDD* calculations, we estimated high-resolution locations of February 2023 main and aftershocks that occurred in SE Türkiye (Figure 3).

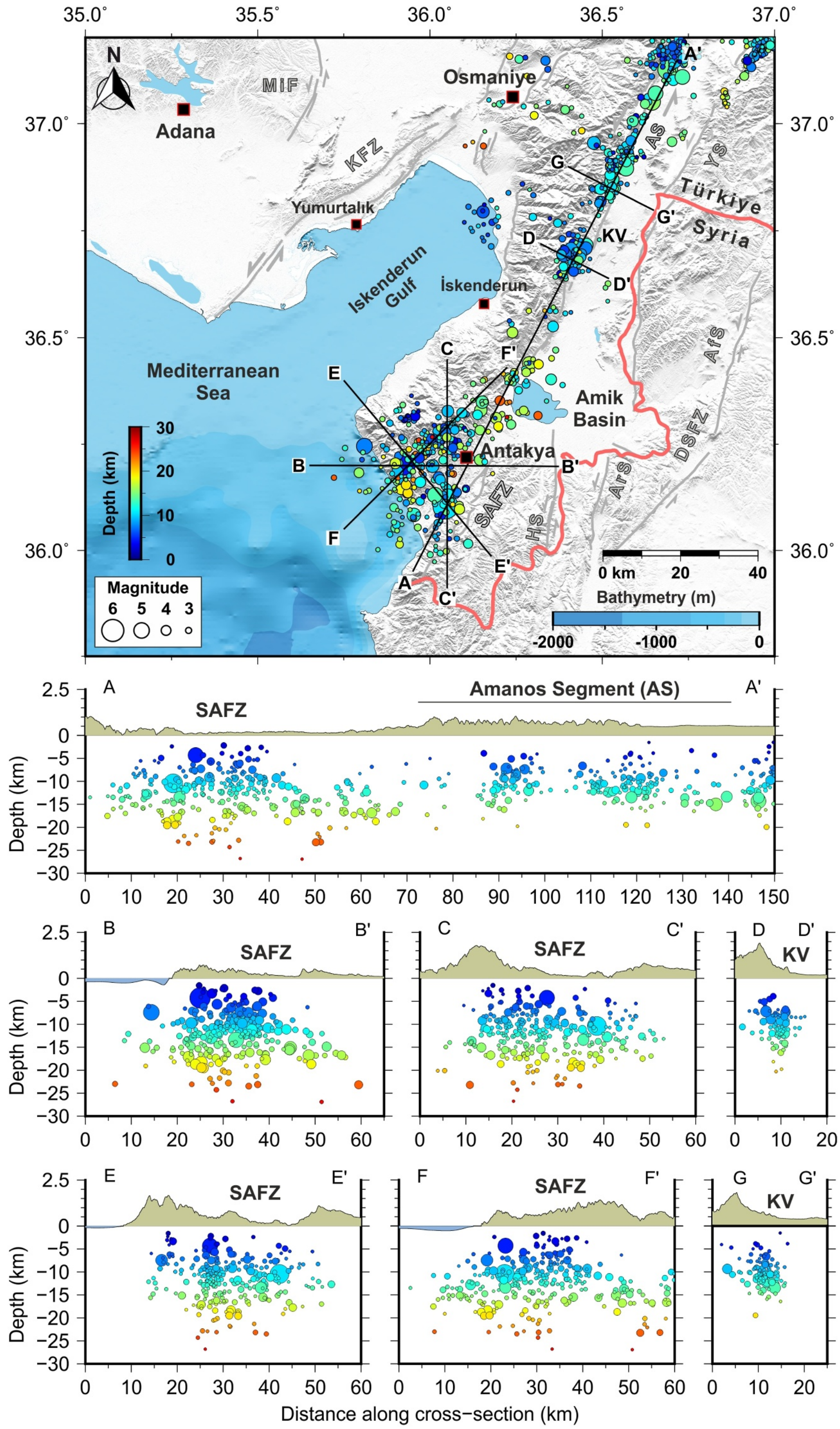

Figure 3. The relocated epicenters of the Hatay-Syria earthquake sequence between the 6 February 2023 and 8 May 2023. Active faults are taken from Emre et al. (2012, 2013, 2018) and Duman and Emre (2013). The size of the circles is scaled by the magnitude, and they are colored by their focal depths. The vertical cross-sections taken along the seven different directions are plotted to indicate the depth variations of the earthquake sequence. Topography is displayed on top of each cross-section. *Abbreviations*: AfS, Afrin Segment; ArS, Armanaz Segment; AS, Amanos Segment; DSFZ, Dead Sea Fault Zone; HS, Hacıpaşa Segment; KFZ, Karataş Fault Zone; KV, Karasu Valley; MiF, Misis Fault; SAFZ, Samandağ-Antakya Fault Zone.

3.2. Point-Source *P*- and *SH*- Teleseismic Body Waveform Inversion

We obtained source parameters of the 20 February 2023 *Mw* 6.4 Hatay earthquake by inverting teleseismic long-period 31 *P*- and 14 *SH*- and broadband *P*- displacement waveforms. *MT5* (Moment Tensor 5) algorithm of McCaffrey et al. (1991) and Zwick et al. (1994) for the point-source double-couple body-waveform inversion that is based on a comparison of the amplitudes and shapes of the observed and synthetic waveforms was used in this study. It assumes that an earthquake source can be represented as a point in space, but not in time. For this moderate size earthquake, we used eight overlapping isosceles triangles with a rise time of 1.0 s for describing the source time function (STF). Before the inversion, velocity responses were de-convolved from the records and then we re-convolved them with the response of old WWSSN 15–100 long-period instruments that have a suitable bandwidth for the resolution of shallow, moderate-sized events (McCaffrey & Nábělek, 1987; Tan & Taymaz, 2006). A simplified half-space 1D crustal velocity model given by Zwick et al. (1994) for teleseismic waveform modeling was used for the Green's function calculation. Theoretical arrival times of seismic phases were calculated based on the Jeffreys–Bullen travel-time tables (Jeffreys & Bullen, 1958). We also verified the minimum misfit solution by visually analyzing the distribution of *P*- wave first motion polarities on the focal spheres, that are recorded by near-field, regional and teleseismic stations. Unfortunately, we could not obtain the best-fitting solution of the 20 February 2023 *Mw* 5.2 Hatay earthquake from teleseismic *P*- and *SH*- waveform inversion due to the poor data quality with low S/N ratios. However, we analyzed the existing *P*-wave first motion polarities with the *FOCMEC* algorithm (Snoke et al., 1984) to estimate the faulting geometry of this aftershock. Additional information about the methods and following procedures for estimating uncertainties of source parameters can be found in McCaffrey and Abers (1988), Taymaz et al. (1991, 2021), Taymaz, Ganas, et al. (2022), Taymaz, Yolsal-Çevikbilen, et al. (2022), Maggi et al. (2000), Yolsal-Çevikbilen & Taymaz (2012, 2019), and in Supporting Information S1.

3.3. Time-Domain RMT Inversion

We implemented the Time Domain Moment Tensor Inversion technique (*TDMT_INVC*) of Dreger and Helmberger (1993) to acquire the source parameters of the 20 February 2023 *Mw* 6.4 and *Mw* 5.2 Hatay earthquakes. The least squares approach of Dreger and Helmberger (1993) and Dreger (2003) was used for inversion of the seismic moment tensor, which has been proven to be reliable for events with local magnitudes (M_L) as small as 3.5. We analyzed three-component body waveforms recorded by broadband and strong ground-motion stations at local and regional distances (Figure S3 in Supporting Information S1; 104–409 km for the *Mw* 6.4 and 30–32 km for the *Mw* 5.2 earthquakes). First, the linear trend of the data was removed, and the data was converted into displacement utilizing the related instrument responses of each seismic station. After tapering and rotating them into radial, transverse and vertical components, we filtered the waveforms of 2023 *Mw* 6.4 event between 0.01 and 0.05 Hz, and the *Mw* 5.2 aftershock waveforms between 0.05 and 0.1 Hz, following the methodology described in Dreger et al. (1995) and Pasyanos et al. (1996). Additionally, we re-sampled the waveforms to 1 s for both events. The seismic source was assumed to be represented by a deviatoric solution that can be decomposed into a double-couple (DC) and a CLVD, while the volume changes (isotropic component) are not resolved. The STF was assumed to be a Dirac delta function (Dreger, 2003). The source depth was found iteratively by finding the solution that yields the largest variance reduction (VR). The Green's functions were calculated using a modified Haskell algorithm (*FKRPROG*) in the frequency-wavenumber domain (Saikia, 1994). The sampling rate was fixed at 1 Hz. We used an average 1-D velocity model representing the source area (Dreger, 2003; Kalafat et al., 1987) for the forward prediction of synthetic waveforms. The quality of the inversion was checked by several parameters such as double-couple percentage (DC%) and VR that is known as the goodness-of-fit parameter calculated between the observed and synthetic waveforms (Pasyanos et al., 1996; Templeton & Dreger, 2006). The other details of the processing steps can be found in the articles of Çubuk et al. (2014), Irmak (2013), Irmak et al. (2020, 2021), Taymaz, Ganas, et al. (2022), and Taymaz, Yolsal-Çevikbilen, et al. (2022).

3.4. Kinematic Finite-Fault Slip Inversion

To model the spatial co-seismic slip distribution and time evolution of the 20 February 2023 *Mw* 6.4 Hatay earthquake, we used the kinematic slip inversion algorithm of Yagi & Kikuchi (2000) and Yagi et al. (2012, 2014). A finite-fault slip model of this earthquake was estimated from a joint inversion of 36 teleseismic broadband *P*-wave displacement and 21 near-field strong ground motion (SGM) data, as well as from a separate

10.1029/2023GC011353

inversion of 40 teleseismic broadband *P*-wave velocity data. For both inversions, seismic stations were carefully selected so as to provide a good azimuthal coverage on the focal sphere for constructing a stable finite-fault slip model of the earthquake. We set the input parameters of the slip inversion (e.g., strike and dip angles of the fault, focal depth, rise time) considering the inversion result of point-source *P*- and *SH*- body waveform modeling. The strike, dip angles, and focal depth were established as fixed, while the rake angle was allowed to change ±25° in the inversion. We assumed that faulting occurs on a single fault plane and rupture started at the hypocenter. The rupture process was presented as a spatiotemporal slip distribution on a fault plane, which was divided into $M \times N$ sub-faults with length dx and width dy. To define the optimum fault dimensions, we checked numerous initial models with varied grid-sizes (*dx, dy*), and numbers of sub-faults in numerical test inversions. We also considered the spatial distribution of relocated aftershocks in the study area. For joint slip inversion, the NE-SW oriented fault plane was divided into 12 × 5 sub-faults along the strike and dip directions with a cell size of 3 km × 3 km, respectively. The hypocenter was located at 7 × 3 grid cells at a depth of 12 km that was presented by a white star on the slip model. The slip-rate function of each sub-fault was composed of seven overlapping isosceles triangle functions with a rise time (τ) of 1.0 s.

We manually picked the *P*- wave first arrivals to estimate an alternative slip model with the inversion of only teleseismic *P*- velocity waveforms. Before the inversion, theoretical Green's functions with a sampling rate of 0.1 s were calculated using the method of Kikuchi and Kanamori (1991) and the Preliminary Reference Earth Model (*PREM*; Dziewonski & Anderson, 1981). We divided the fault plane into 180 sub-faults with 18 × 10 sub-faults along the strike and dip directions, respectively, and the area of each sub-fault cell size was set as 2 km × 2 km. We positioned the hypocenter at 10 × 5 grid cells at a depth of 12 km, and we defined the slip-rate function of each sub-fault that was composed of six overlapping isosceles triangle functions interpolated with linear B-splines with a rise time (τ) of 1.0 s. In addition, we presumed the rupture velocity (*Vr*) to be 3.2 km/s after performing a series of inversions with a constant *Vr* ranging from 2.5 to 3.4 km/s. For each inversion, we checked the variance value of the inversion result, and accepted the optimum slip model by considering the minimum variance value. We also applied smoothing constraints to the slip distribution with respect to time and space in order to avoid the instability, which may occur when there are many unconstrained parameters in an inversion. In this study, an optimized ABIC, *the Akaike's Bayesian Information Criteria* (Akaike, 1980; Fukahata et al., 2003; Yagi & Fukahata, 2011; Yagi et al., 2004; Yoshida, 1992) was used to determine the smoothness parameter for the inversion process. Average slip on the fault plane was then calculated susing the size of the fault plane, seismic moment and conventional equations of Aki (1972) and Kanamori (1994). More comprehensive information about the finite-fault slip inversion procedures can be found in earlier studies (e.g., Fielding et al., 2013; Taymaz et al., 2021; Taymaz, Ganas, et al., 2022; Taymaz, Yolsal-Çevikbilen, et al., 2022; Yagi et al., 2012, 2014; Yolsal-Çevikbilen & Taymaz, 2019; Yoshida et al., 1996).

3.5. Moment Magnitude Estimation From Coda Wave Analysis

This work also examines the seismic moment and moment magnitude (Mw) associated with the 20 February 2023 (OT: 17:04:27 UTC) Hatay earthquake using a comprehensive analysis of coda waves. To achieve this, we adopted a methodology originally developed by Sens-Schönfelder and Wegler (2006), and further refined it in Eulenfeld and Wegler (2016). The approach involves an iterative inversion process where we progressively minimize the differences between observed and synthetic envelope data to simultaneously model the effects of the geological site, seismic wave propagation path, and earthquake source characteristics (e.g., Eken, 2019). The analytical expression of the coda wave approach during forward calculation relies on the principles of Radiative Transfer Theory. This theory is based on the computation of energy density within a specific frequency range, assuming an isotropic seismic source, as originally outlined by Sens-Schönfelder and Wegler (2006). The outcomes of the coda envelope inversion process include various source-and structural parameters. These are the frequency-varying spectral source energy term (W_j), the site response (R_i), and the parameters related to intrinsic (b) and scattering attenuation (g). We gathered coda wavefield data observed on the digital waveform recordings of seven permanent broadband stations operated by BU-KOERI.

3.6. GNSS Data Analysis

The GNSS is one of the most efficient techniques for monitoring deformation and tectonic movements and determining the co-seismic displacements because it can provide highly accurate position information in all weather conditions and 24 hr a day. Conventionally, the Relative Point Positioning (RPP) technique is preferred to analyze GNSS observations by establishing a network structure. Since the differencing observation is used to eliminate GNSS errors (e.g., orbit and clock errors and atmospheric delays), other effects such as local deformations on the reference station(s) can affect the analysis and lead to incorrect interpretations. Over the last two decades, another technique, the so-called Precise Point Positioning (PPP) technique, has emerged to determine precise positions of stations using a single GNSS receiver (Zumberge et al., 1997). However, in this technique, longer observation durations and precise orbit and clock products are required to achieve precise positioning. It has been shown in the literature that the PPP technique might be preferred to determine the displacements, and tectonic movements, and also to monitor deformations. For instance, Larson and Miyazaki (2008) analyzed high-rate GPS observations to determine the co-seismic and post-seismic deformations for the 2003 *Mw* 8.3 Tokachi-Oki earthquake. P. Xu et al. (2013) showed that high-rate PPP is capable of detecting absolute seismic displacement waveforms with the same high accuracy as RPP. Martin et al. (2015) investigated the usability of real-time kinematic PPP for deformation monitoring, and they concluded that this technique can be an efficient tool for monitoring the deformations. Dogan et al. (2018) further reported that the PPP technique with both static and kinematic solutions gives applicable results for detecting the displacements during the 21 July 2017 *Mw* 6.6 Kos-Bodrum earthquake. In this study, PPP technique was preferred when analyzing GNSS observations to determine co-seismic displacements using an online GNSS data processing service, the so-called Canadian Spatial Reference System Precise Point Positioning (CSRS-PPP). The service uses precise satellite ephemerides, clock products, and satellite phase biases provided by NRCan/IGS services with dual-frequency GNSS observations. Moreover, the updated version of the service (as of 20 October 2020) has included PPP with ambiguity resolution (PPP-AR) for carrier phase observations (Ocalan et al., 2022).

4. Results

Here, our main findings obtained from the conventional modeling approaches based on seismological and geodetic data and observations are presented. Besides, some of the results are given in Supporting Information S1 in detail.

4.1. Relocated Earthquakes

The distribution of 777 relocated earthquakes that occurred along the segments of the EAFZ (e.g., Amanos, Yesemek segments) and SAFZ between the time period of 6 February 2023 and 8 May 2023 in the Hatay-Syria area (Lat: 35.75°–37.20°N, Lon: 35.00° −37.00°E) are presented in Figure 3. Among them, 23 events have a magnitude greater than 4.0, and three of the earthquakes have a magnitude greater than 5.0. On 20 February 2023, there are 52 notable earthquakes ($M > 2.5$) occurred in our study region, including the 2023 *Mw* 6.4 Hatay earthquake (Figure 1). We obtained the relocated hypocenter of the *Mw* 6.4 earthquake at a latitude of 36.103°N and a longitude of 36.045°E at a depth of 10.43 km from the detailed analysis with *hypoDD* algorithm. We also relocated its major aftershock (*Mw* 5.2) that occurred on 20 February 2023 at the NW of the earthquake with epicentral coordinates of 36.210°N and 35.930°E (Table 1). To better underline the rupture extent along-dip direction and the spatial distribution of relocated aftershock clusters, we prepared 7 vertical cross-sections along various directions as labeled from A-A′ to G-G′. Subsequently, we examined the geometric orientation of the fault segments and correlation between earthquake clusters and tectonic features in the study area (e.g., major fault segments, valleys as such) (Figure 3).

In general, earthquakes show a distinct pattern of clustered linear distribution that allows us to establish the geometry of the re-activated fault segments around the Antakya-Hatay region. The vertical cross-sections of the relocated aftershocks predominantly exhibited a seismogenic depth shallower than 25 km in the region. Most of the earthquakes appear to concentrate on the depth range of 10–20 km of the crust (Figure 3).

4.2. Earthquake Source Characteristics From Body-Wave Inversions

The source parameters of the 20 February 2023 Hatay *Mw* 6.4 earthquake obtained from point-source double-couple teleseismic, RMT and kinematic slip inversions are summarized in Table 3. Further, the estimated Mw from coda-wave analysis for this earthquake is given in this table. We resolved reliable source parameters of the *Mw* 6.4 earthquake from the inversion of teleseismic long-period 31 *P*- and 14 S*H*- waveforms (Figure 4),

10.1029/2023GC011353

Table 3
Source Mechanism Parameters of the 20 February 2023 Mw 6.4 Hatay Earthquake Obtained From This Study

The 20 February 2023 *Mw* 6.4 Hatay earthquake (Lat: 36.103°N—Lon: 36.045°E—OT: 17:04:27 UTC)				
	Faulting geometry		Finite-fault slip model	
Source parameters	Point-source double-couple	Regional MT	Joint inversion (Tele P + SGM)	Teleseismic *P*- only
Strike (ϕ, °)	208	220	208[a]	208[a]
Dip (δ, °)	30	38	30[a]	30[a]
Rake (λ, °)	−28	−21	−24	−20
Focal depth (km)	12	12	12[a]	12[a]
Fault length (L, km)	–	–	36	36
Fault width (W, km)	–	–	15	20
Maximum slip (cm)	–	–	100	60
Average slip (cm)			22	10
Seismic Moment, Mo ($\times 10^{18}$ Nm)	5.178	5.400	3.518	2.092
Stress drop, $\Delta\sigma$ (bars)	–	–	7	3
Mw	6.4	6.43	6.3	6.2
Mw 6.2 from coda wave analysis				

Note. The relocated epicenter coordinates and origin time of the earthquake are estimated by this study. [a]Denotes the input parameters of the kinematic finite-fault slip inversion, which are estimated from the point-source minimum misfit solution, and are kept fixed in the inversion.

but we could not obtain an optimal source mechanism solution of the 2023 *Mw* 5.2 aftershock due to the inadequate number of teleseismic data with good S/N ratios that disabled reasonably good matching between observed and predicted data. Likewise, the Mw of this aftershock could not be estimated from the coda wave analysis.

It is seen from Figure 4 that the azimuthal distribution of teleseismic stations on the focal sphere was adequate to estimate a reliable solution for *Mw* 6.4 earthquake. The inversion result indicates an oblique slip faulting mechanism consistent with the general tectonics of the region. It primarily revealed a NE-SW oriented fault plane with a strike (ϕ) of 208° ± 5°, a dip (δ) of 30° ± 5° and a rake angle (λ) of −28° ± 5°. The focal depth, seismic moment (M_o) and source duration of this event were estimated to be 12 ± 2 km, 5.178×10^{18} Nm and about 10 s, respectively. This solution was characterized by an R/D ratio (percent ratio of residual to data variance) of 27.8% (Table 3 and Figure 4).

Likewise, we observed that this mechanism is consistent with the azimuthal distribution of *P*- wave first-motion polarities on the focal sphere. Some of the stations efficiently constrained the nodal planes as they were located very close to both nodal planes (e.g., up motions at DIV, IPM, KBS, ANTO stations). The downward *P*- wave motions on the waveforms were also rather apparent at stations located in the dilatation part of the focal sphere (see EIL, TAM, MACI, KMBO; Figure 5).

Consistently, RMT solutions of both earthquakes exhibited a normal faulting mechanism with a significant amount of left-lateral strike-slip component at a shallow focal depth of 12 km (Figures S5 and S6 in Supporting Information S1; Tables 1 and 3). The RMT solution of 2023 *Mw* 6.4 earthquake was relatively well-constrained by a DC% of 86 and a VR value of 64%. However, we cannot claim a robust solution for its largest aftershock as it is characterized by 61% DC and poor error minimization (e.g., VR of 44.5%) mainly due to the lack of the reliable waveforms with a good quality signal (Table 3; Figures S5 and S6 in Supporting Information S1). We approximately calculated a *Mw* of 5.2 for the 20 February 2023 (OT: 17:07:33 UTC) Hatay earthquake (Table 3), while USGS (2023b) and AFAD (2023a) reported an earthquake magnitude of 5.5 for this event.

Since we consider that our RMT solution of this event, which was estimated using only two near-field stations, is controversial, we attempt to constrain the faulting geometry based on a detailed analysis of *P*-wave first motion polarities recorded at regional, local and teleseismic distances. For this purpose, *P*-wave first motions were reliably identified on 20 vertical-component seismograms that have reasonable signal amplitudes, and then they

10.1029/2023GC011353

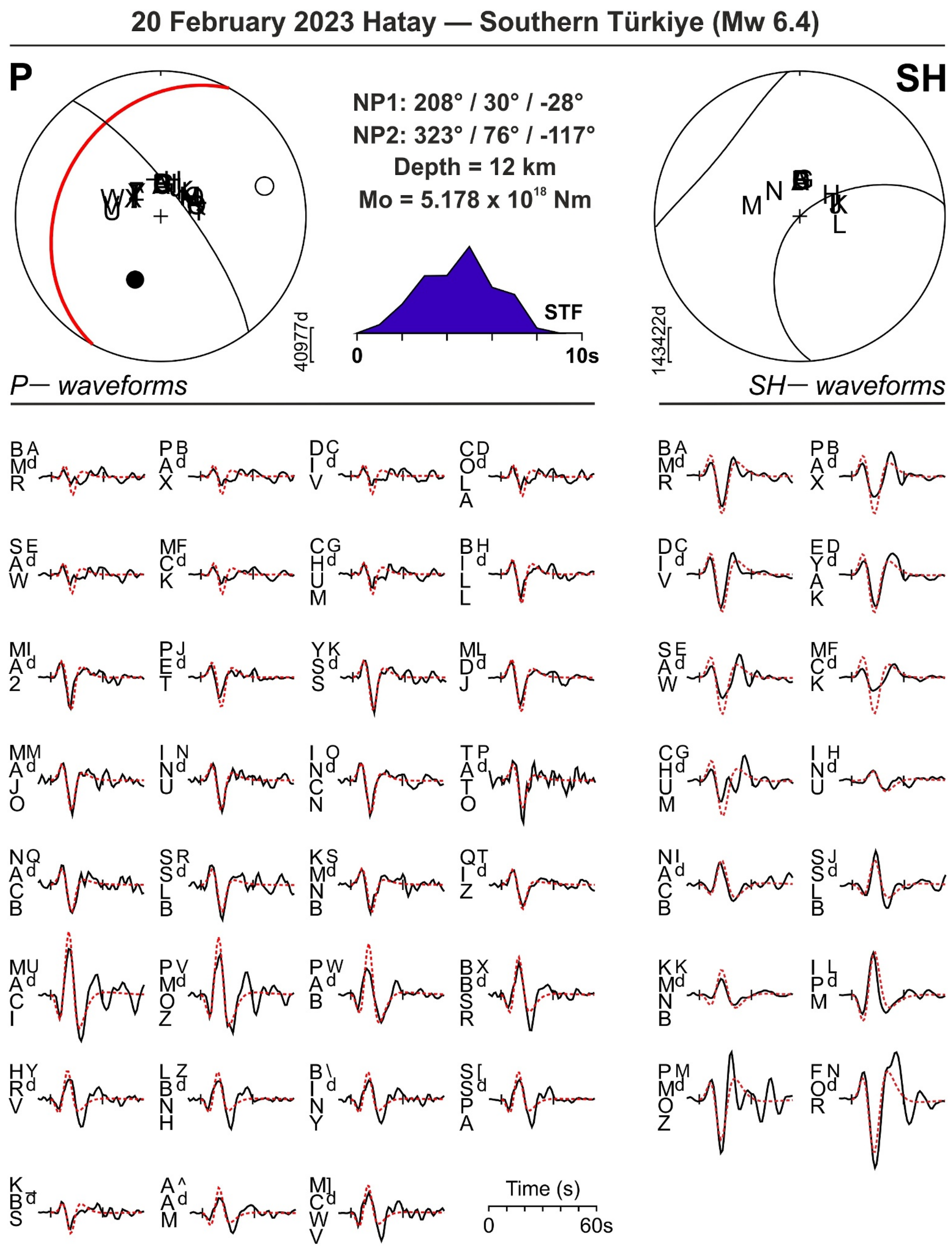

Figure 4. Source mechanism solution of the 20 February 2023 *Mw* 6.4 Hatay (southern Türkiye) earthquake obtained from the double-couple point-source inversion. The dashed red lines indicate synthetic waveform fits to each of the 31 *P*- and 14 *SH*- long-period observed waveforms (solid black lines) used in the inversion. The header at the top of the figure shows the date and moment magnitude along with the strike, dip, and rake angles of the first and second nodal planes (NP), centroid depth (h), and seismic moment (Mo). The source time function is shown beneath the header, while the time scale used for the waveforms is given near the waveforms in the last row of the figure. Focal spheres are shown with *P*- (top) and *SH*- (bottom) nodal planes in lower hemisphere projections. The vertical bar near the focal spheres shows the waveform displacement scale in microns, with the lowercase letter identifying the instrument type (d: GDSN long-period). Station positions are indicated by a capital letter and are arranged alphabetically clockwise, starting from the north. The *P*- and *T*-axes are marked by black and white circles, respectively.

were analyzed using the *FOCMEC* algorithm (see Snoke et al., 1984). We obtained the focal mechanism solution (strike/dip/rake angle: 230°/44°/−24°; Figure S7 in Supporting Information S1) as compatible with fault orientation defined by the RMT inversion (Figure S6 in Supporting Information S1). The RMT solution agrees

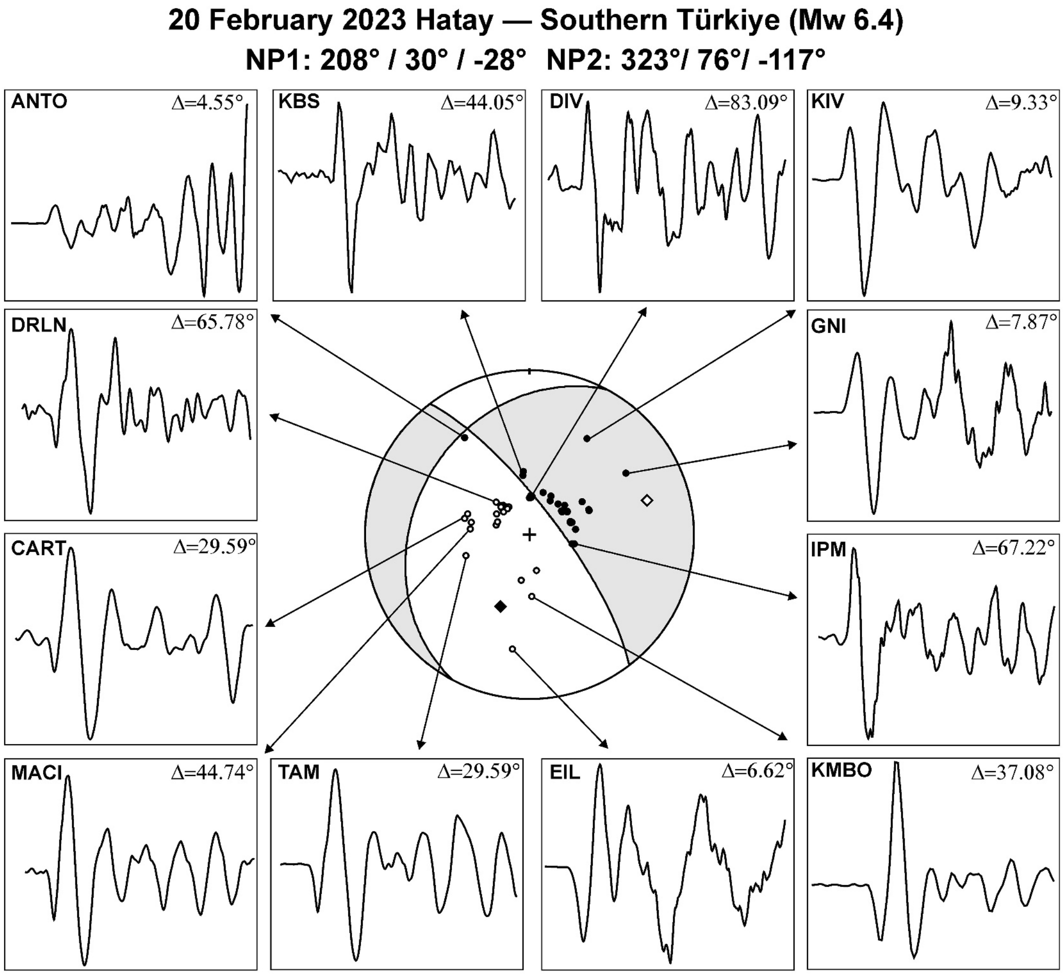

Figure 5. The azimuthal distribution of *P*- wave polarity data, recorded by seismic stations at teleseismic and regional distances, on lower hemisphere equal area projection for the minimum misfit solution of the 20 February 2023 *Mw* 6.4 Hatay earthquake obtained from the point-source inversion in this study. Station positions on the focal sphere have been plotted using the same velocity structure that was used in the inversion procedure. Compressional and dilatational first motions are depicted by closed and open circles, respectively. Station codes and epicentral distances, Δ (°), are given above the waveforms. The *P*- and *T*-axes are marked by black and white diamonds, respectively.

well with the fault geometry estimated from the detailed analysis of *P*-wave first motions, as this indicates that the obtained source parameters can be acceptable for interpretation. The details can be found in the SI file.

Figures 6a–6c presents an example of the coda wave fitting process performed on seven seismic stations. Our primary focus here is to estimate the source term, W_j, which allows us to further determine the source displacement spectrum and moment magnitude of the 20 February 2023 (OT: 17:04:27 UTC) Hatay earthquake. Figure 6c exhibits the predicted model spectrum (see solid black curve) estimated through a curve fitting process (Abercrombie, 1995). This was applied to the modeled frequency dependent spectral amplitudes (solid circles color coded by the number of observations) derived from the resolved spectral source energy term W at each frequency. We determined the seismic moment by examining the flat segment of the source displacement spectra. Our analysis yielded a coda-derived seismic moment of 2.4×10^{18} Nm, corresponding to a Mw of 6.2. We noted that our coda-derived Mw estimate is in good agreement with those obtained through double-couple point-source and finite-fault slip inversions conducted in this study. This agreement indicates the effective usage of local coda waves for modeling of source properties characterized by a flat region and spectral decay behavior, separated at a corner frequency of 1.2 Hz (Figure 6c).

10.1029/2023GC011353

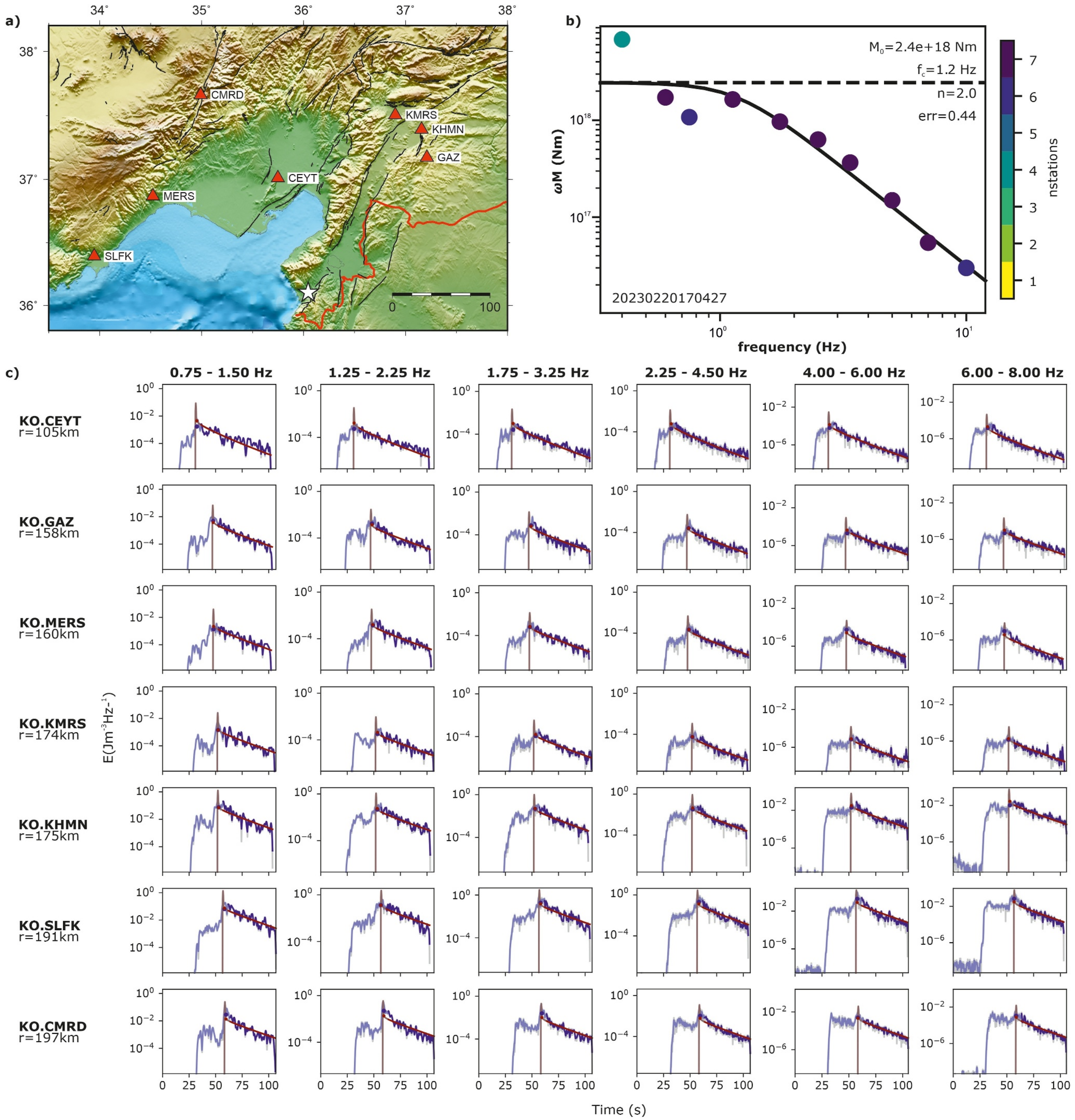

Figure 6. (a) Plots for moment magnitude estimation using the coda wave analysis. The map on the left indicates the epicenter of the 20 February 2023 (OT: 17:04:27 UTC) earthquake (white star) and locations of seven broadband seismic stations shown by red triangles. (b) The actual amplitudes of observed source displacement spectra (solid circles color coded by the number of observations) with its corresponding modeled curve (see solid black curve). The green dot representing the minimum frequency has four observations and is colored to show its down-weighted contribution (c) The figure showing the performance of our coda wave envelope fitting process at five different frequency bands observed for all seven stations.

4.3. Finite-Fault Slip Models Obtained by Kinematic Slip Inversion

4.3.1. Joint Inversion of Teleseismic and SGM Data

From the joint inversion of 36 teleseismic broadband *P*-displacements and 21 strong ground-motion waveforms, we obtained the best finite-fault slip model of the 2023 *Mw* 6.4 Hatay earthquake. During the inversion, we attempted to achieve the best fit for both the onset and the amplitude of the waveforms. We modeled the NE-SW oriented left-lateral fault plane with a 208° strike and 30° NW dip as defined by the *P*- and *SH*- waveform inversions. The obtained model primarily implied a normal faulting mechanism with a significant amount of left-lateral horizontal displacement (Figures 7a–7c).

The inversion result gave a total seismic moment of 3.518×10^{18} Nm (*Mw* 6.3), and a rupture duration of 12 s. The inverted rake angle was −24°, which is fairly consistent with the values from the RMT and *P*- and *SH*- waveform inversions (Table 3). The size of the fault plane was estimated to be 36 km (fault length) × 15 km (fault width). We clearly distinguished a uniform and single asperity involving a maximum displacement of 100 cm close to the hypocenter. The slip vectors refer to a NE-SW oriented rupture propagation with co-seismic horizontal displacements along the strike of the fault plane, and they indicated a notable component of dip-slip displacement that was largely concentrated at the shallow part of the fault plane to the NE of the hypocenter (Figure 7a). A unilateral rupture is evident as the ruptured area is spread predominantly confined to only one side of the hypocenter on the fault plane. The mean displacement on the fault plane and static stress drop of the earthquake were calculated to be 20 cm and 7 bars, respectively (Figures 7a, Table 3).

4.3.2. Inversion of Teleseismic *P*-Wave Velocity Data Only

We also estimated an alternative finite-fault slip model from the inversion of only 40 teleseismic *P*-velocity waveforms. Similar to the joint inversion model, it indicated a unilateral rupture mainly along the strike direction with a maximum displacement of about 60 cm at the NE of the earthquake hypocenter. The model showed a relatively simple rupture, which lasted about 10–12s without producing any surface break. Furthermore, both horizontal and vertical slip motions were evident on the fault plane, which has about 36 km of the fault length and 20 km of the fault width. The vertical downward slip vectors were particularly dominant in the SW part of the fault plane (Figures 8a and 8b). Nevertheless, we estimated a seismic moment (M_o) of 2.092×10^{18} Nm and *Mw* of 6.2 from the inversion of only teleseismic *P*- velocity data (Figure 8). They are slightly smaller than those from the minimum misfit solution and the RMT inversion (Figure 4 and Figure S5 in Supporting Information S1). We estimated the mean displacement on the fault plane and the value of the static stress drop to be 10 cm and 3 bars, respectively (Table 3).

4.4. The Amount of Co-Seismic Displacements From GNSS Data Modeling

The overall distribution of the GNSS stations is reasonably sufficient to record both near-field (e.g., station HATA*) and far-field effects (e.g., station ANTE). The analyzed time series of the available GNSS stations indicated a pattern of co-seismic displacements consistent with the oblique slip kinematics of the rupture. As stated in Section 3.6, station observations were processed using the PPP technique. Although this technique requires a longer session duration than RPP to achieve a precise position, depending on the session duration, cm to mm level accuracy can be achieved (Teunissen, 2021). We obtained significant vertical displacements of −2.64 and 1.87 cm at near-field stations HAT2 and ARST, respectively. The noteworthy horizontal co-seismic displacements were only observed at two stations: −1.81 cm (HATA*) and −1.03 cm (HAT2) located in Hatay province. However, the results revealed rather large uncertainties in the calculations from the time series of the GNSS stations. The obtained displacements and their standard deviations for each station are summarized in the Table S7 in Supporting Information S1 and Figure 9.

Moreover, we analyzed kinematic time series from the three stations closest to the epicenter of the *Mw* 6.4 earthquake, namely HATA, HAT2 and ARST. Since there were no observations at HATA at the time of the earthquake, the kinematic results for this station were not presented. As it can be seen from Figure 9, the displacements obtained for ARST are approximately 5 cm in the east and north components. Furthermore, for the HAT2, the observed displacements are about 15 and 10 cm in the east and north components, respectively (Figure 9).

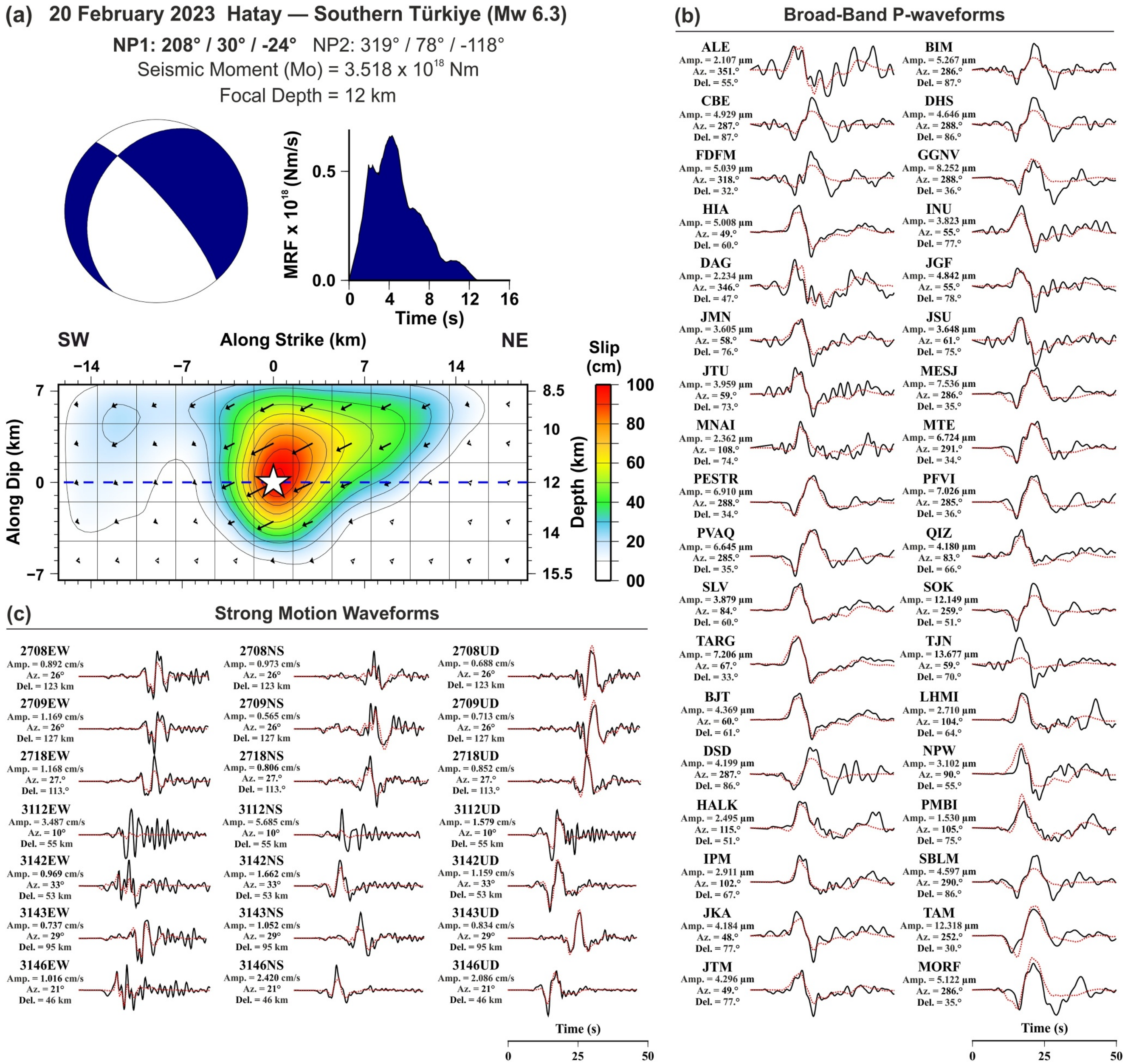

Figure 7. (a) Focal mechanism, co-seismic slip distribution and total moment rate function of the 20 February 2023 *Mw* 6.4 Hatay earthquake obtained from the joint inversion of teleseismic and strong ground-motion data. The strike, dip and rake angles of the first and second nodal planes (NP) and focal depth obtained from the minimum-misfit point-source solution are given in the header. The slip model is derived on NP1. The white star with blue dashed line shows the location of the initiation of the rupture located at a focal depth of about 12 km (origin of the plot axes) obtained from minimum misfit solution. The slip vectors and the distribution of slip magnitudes are also presented. Along-strike distances are shown on the top *x* axis, along-dip distances on the left *y* axis and depth beneath the surface on the right *y* axis. The vertical-colored scale given on the right side shows the amount of slip values in cm, (b) Comparison of the observed (black solid lines) and synthetic (red dashed lines) broadband 36 *P*- displacement waveforms used in the joint finite-fault slip inversion. The peak amplitude of the observed ground displacement is in μm, (c) Comparison of the observed (black) and synthetic (red) 21 strong ground-motion waveforms used in the joint slip inversion. The peak amplitude of the observed ground velocity is in cm/s. Station code, maximum amplitude, station azimuth and distance are given near the waveforms. The time scale used for the waveforms is shown in seconds at the bottom.

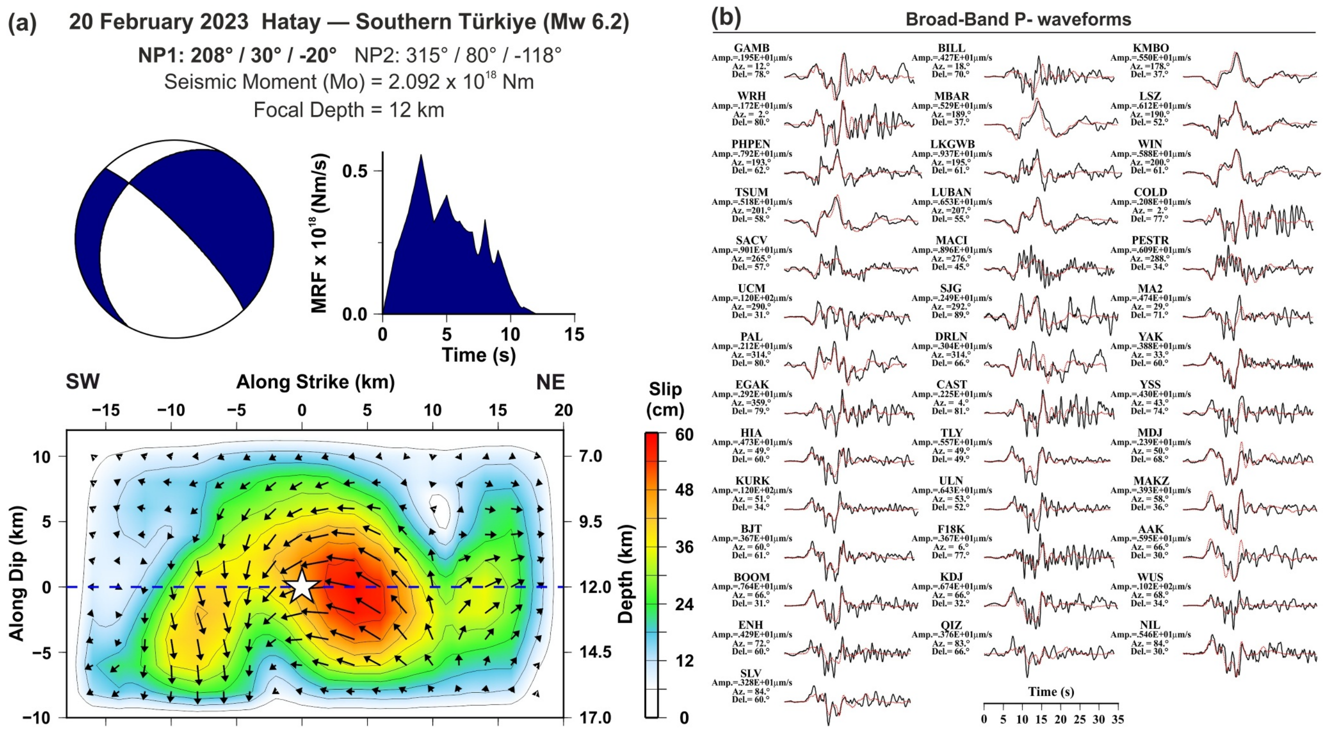

Figure 8. (a) Focal mechanism, co-seismic slip distribution and total moment rate function of the 20 February 2023 *Mw* 6.4 Hatay earthquake obtained from finite-fault slip inversion with only teleseismic *P*- velocity data. The other details are as in Figure 7a. (b) Comparison of the observed (black) and synthetic (red) teleseismic broadband 40 *P*- velocity waveforms used in the finite-fault slip inversion. Station code, maximum amplitude, station azimuth and distance are shown near the waveforms. The peak amplitude of the observed ground velocity is in μm/s. The time scale used for the waveforms is shown in seconds at the bottom.

5. Discussion

5.1. Relocated Aftershocks and Source Characteristics of the 2023 Hatay Earthquakes

The source and rupture characteristics of the 20 February 2023 *Mw* 6.4 and *Mw* 5.2 Hatay earthquakes and the relocated aftershocks that occurred over a 3-month period were examined to better understand the kinematics of co-seismic rupture evolution and its relationship to the extent of the ruptured fault segments in the study area. It is clear that these events are the aftershocks of the 6 February 2023 *Mw* 7.8 Nurdağı-Pazarcık and *Mw* 7.6 Ekinözü (Kahramanmaraş) earthquakes that ruptured the Pazarcık and Çardak-Sürgü segments of the EAFZ in the northeast. This can be corroborated by several seismic activity that occurred along the AS and SAFZ between 06 February 2023 and 19 February 2023 (see earthquakes shown by red circles in Figure 10). In addition, the aftershock area (e.g., up to a distance equal to the rupture length of the mainshock), the observed decay rate and the possible largest magnitude of these aftershocks agree well with the general definitions of the Bath, Utsu-Omori and Gutenberg-Richter laws (Bath, 1965; Gutenberg & Richter, 1954; Omori, 1894; Utsu, 1961). From the teleseismic *P*- and *SH*-waveform modeling and RMT inversions, we estimated a normal faulting mechanism with a significant amount of left-lateral strike slip component for both earthquakes (Figure 4; Figures S5 and S6 in Supporting Information S1). Unfortunately, we could not estimate reliable source parameters for the 20 February 2023 *Mw* 5.2 aftershock from waveform inversions because most of the waveforms were significantly distorted by the seismic phases released by the *Mw* 6.4 earthquake that occurred 3 min earlier. However, analysis of *P*-wave first motion polarities recorded by stations at near-field, regional and teleseismic distances (Figure S7 in Supporting Information S1) provide us a fault geometry compatible with the results of RMT inversion for both events (Figures S5 and S6 in Supporting Information S1).

In addition, our slip models of the *Mw* 6.4 earthquake, derived from the joint inversion of teleseismic *P*- and SGM data and from teleseismic *P*-data only, consistently showed a simple slip distribution pattern and rupture propagation on the fault plane. They indicated a large amount of slip, which mainly concentrated to the NE of the earthquake hypocenter (Figure 10). We also resolved a single circular-shape asperity with dominant oblique slip

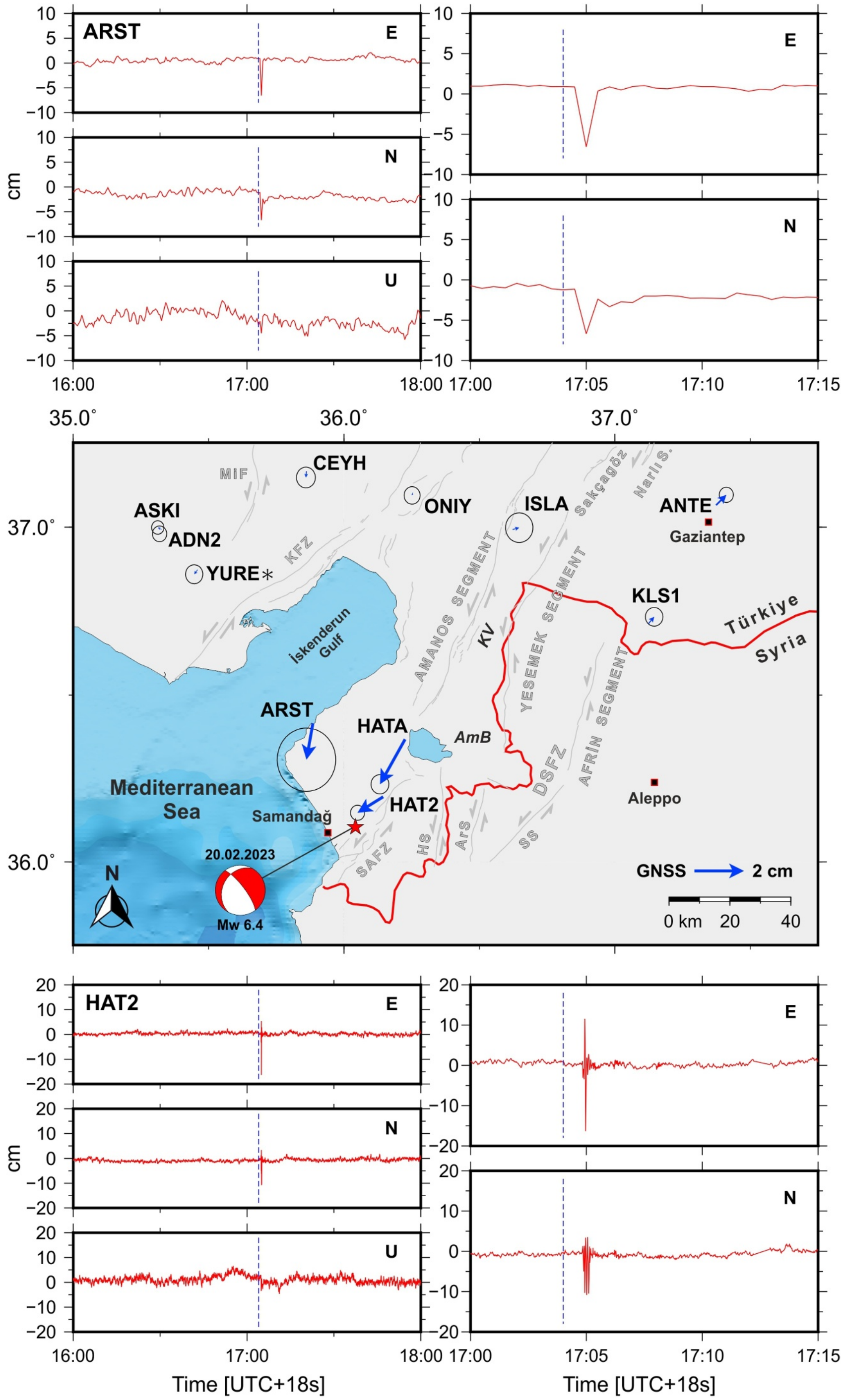

Figure 9. Examples of the analyzed kinematic time series of available Global Navigation Satellite System (GNSS) stations (e.g., ARST and HAT2; see above and below the map) and distribution of the analyzed GNSS stations displaying co-seismic horizontal displacements (indicated by blue arrows) resulted from the 20 February 2023 *Mw* 6.4 Hatay earthquake (marked by a red star). The focal sphere indicates the source mechanism solution of the earthquake obtained in this study. The GPS error ellipses exhibit a 67% confidence interval (Table S7 in Supporting Information S1). The active faults are taken from Emre et al. (2012, 2013, 2018) and Duman and Emre (2013). *Abbreviations*: AmB, Amik Basin; ArS, Armanaz Segment; DSFZ, Dead Sea Fault Zone; HS, Hacıpaşa Segment; KFZ, Karataş Fault Zone; KV, Karasu Valley; MiF, Misis Fault; SAFZ, Samandağ-Antakya Fault Zone; SS, Sermada Segment.

on the fault plane with a maximum displacement of 60–100 cm located at about NE of the hypocenter, and a unilateral rupture on the fault plane of the earthquake. An average rake angle of about −24° was estimated from the inversions performed with various-scale seismological data in this study (Table 3). This confirmed that the

10.1029/2023GC011353

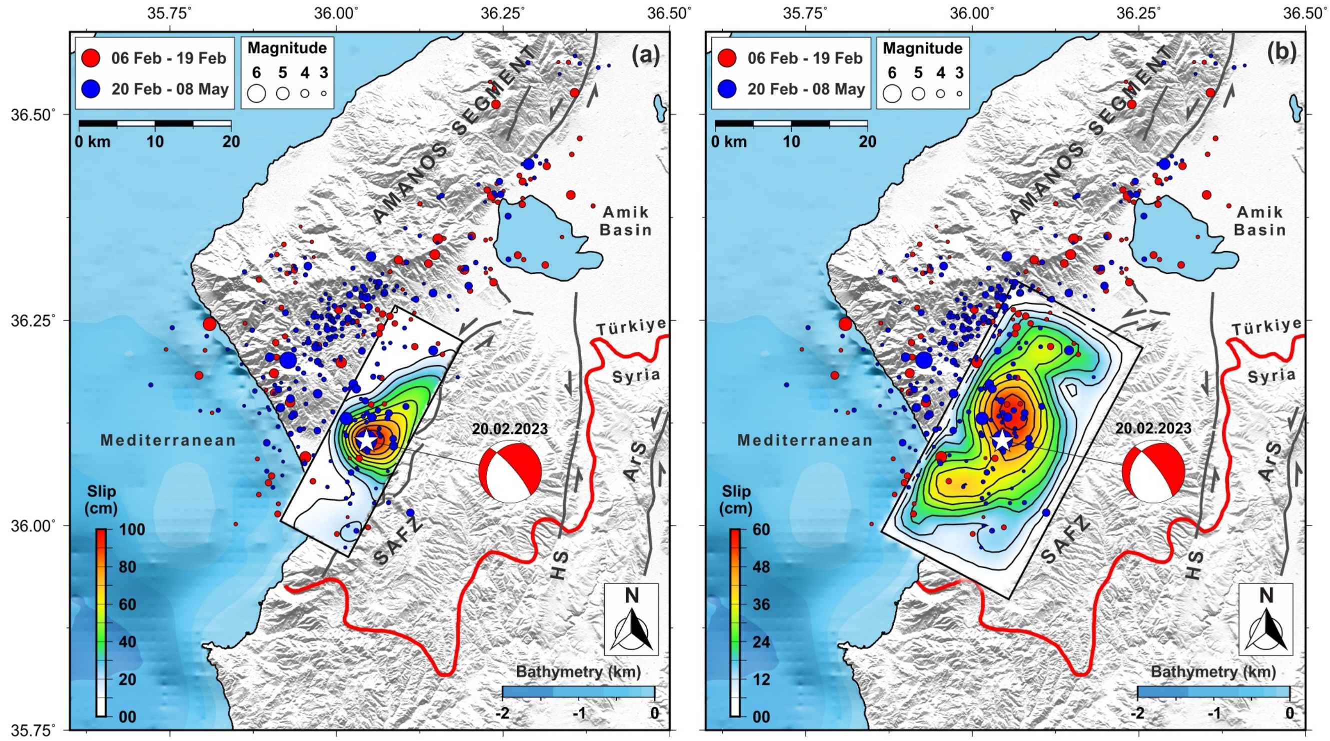

Figure 10. (a) Map-slip presentation obtained from joint inversion of teleseismic and strong ground-motion data, and (b) slip inversion of teleseismic *P*- data only. The relocated aftershocks scaled by their magnitudes are shown in red and blue circles. The red and blue circles refer to relocated aftershocks in this study for the period of 6 February 2023–19 February 2023 and 20 February 2023–8 May 2023, respectively. The active faults reported by Emre et al. (2012, 2013, 2018) and Duman and Emre (2013) in the study area are plotted as gray lines. *Abbreviations*: ArS, Armanaz segment; HS, Hacıpaşa Segment; SAFZ, Samandağ-Antakya Fault Zone.

main segments of the EAFZ, the DSFZ and the Cyprus arc in the Hatay-Syria region represent a continuation of a transform plate boundary between the Anatolian, Arabian and African plates by implying a prominent strike-slip shear zone associated with extensional deformation, as suggested by previous studies (e.g., Kempler & Garfunkel, 1994; Över et al., 2002, 2023). Both indicated a comparable size of the rupture area (approximately 700 km^2), which was further well constrained by the spatial distribution of the relocated aftershocks. Consequently, we proposed that the rupture of about 30–35 km long did not sufficiently reach the Eastern Mediterranean Sea region with a notable amount of displacement as seen in Figure 10, and therefore this earthquake could not generate tsunami waves at the nearby coastal plains as verified by field observations.

Besides, we obtained the best fit between the observed and synthetic waveforms and stable inversion results with a rupture velocity of 3.0–3.2 km/s. The reasonably small static stress drop values (about 3–7 bars) can be recognized as a feature of the inter-plate earthquakes (Kanamori & Anderson, 1975). We also found that our slip models are fairly consistent with the slip model of Barbot et al. (2023), which was estimated from a joint inversion of ascending and descending interferograms based on SAR images. They observed a rupture extending along the strike direction of the 25-km long fault with a maximum slip of 0.93 m at a depth of about 8 km in the NE part of the fault plane (Figure 10).

From the lateral distribution of the relocated earthquakes, we found that several NE-SW striking segments of the EAFZ (e.g., AS, SAFZ), Cyprus arc and DSFZ were involved in the co-seismic rupture processes of the 2023 Hatay-Syria earthquakes. Several linear and fault-parallel (NE-trending) aftershock clusters (see cross-sections of A-A′, B-B′, C-C′, D-D′, F-F′, and G-G′) were apparently observed along the segments of EAFZ and DSFZ, and they can be correlated with the 2023 *Mw* 7.8 Nurdağı-Pazarcık, *Mw* 7.6 Ekinözü and *Mw* 6.4 Hatay earthquakes (Figure 3). It appears that intense earthquake activity mostly clustered at the northwest of the 2023 Hatay epicenter during the time period from 20 February 2023 to May 8, 2023 (blue circles in Figure 10). Since a large number of earthquakes were located away from the 2023 *Mw 6*.4 rupture, we suggest that they may have been due to the triggering of the fault segments already stressed by their neighboring faults (e.g., the Amanos segment of the EAFZ) after the 2023 *Mw* 7.8 and *Mw* 7.6 earthquakes (Figures 1 and 3). The apparently isolated NE-SW trending aftershock clusters located at northeast of the study area (see D-D′, G-G′) may primarily belong to the 6 February 2023 *Mw* 7.8 Nurdağı-Pazarcık earthquake that ruptured the Pazarcık segment of the EAFZ (Figure 3). The NW-dipping left-lateral segment of the SAFZ was obviously defined by the vertical cross-section taken along the E-E′. In addition, another NE-SW trending linear aftershock cluster (see F-F′) positioned at the NW of the 2023 *Mw* 6.4 Hatay epicenter seems more compatible with the strike of the Larnaka ridge segment of the Cyprus arc. We suggest that this cluster shown in F-F′, may be caused by reactivation of the segments of the SAFZ and Latakia-Larnaka ridges along the Cyprus arc due to the calculated stress accumulation after the large 2023 SE Türkiye earthquakes by Toda et al. (2023) (Figures 1 and 3). However, it can be seen that a relatively small number of aftershocks occurred on the fault plane of the 2023 Mw 6.4 Hatay earthquake. The area of somewhat lower and distributed earthquake activity on the southern part of the fault plane, mostly associated with the other segments of the EAFZ and DSFZ, could be defined as a seismically quiescent region undergoing recent stress accumulation. We think that these segments in the Hatay-Syria region will define the potential future earthquake zones.

We further observed that the focal depths of the earthquakes in the study region are generally rather shallow ($h \leq 30$ km) (Table 1). The depth distribution of aftershocks clearly indicates a seismogenic zone at about 20 km depth along the SAFZ. This shallow depth is almost equal to half of the crustal thickness of about 40 km along the EAFZ (e.g., Confal et al., 2020; Vanacore et al., 2013; Zor et al., 2003). Furthermore, an apparent low *P*- velocity zone (2%–3%) at a depth range of 4 and 21 km along the EAFZ and BZSZ was obtained by H. Wang et al. (2020) from the 3D local earthquake tomography study. This low velocity zone following the tectonic structures disappears at a depth of 32 km, and in particular, the south of the EAFZ was represented by the high *Vp* anomalies after this depth. Many studies have indicated that most earthquakes usually occur in the transition zones between the low and high *P*-wave velocity anomalies by considering the locations of rupture zones in many tectonically complex regions (e.g., Cheng et al., 2016; Taymaz et al., 2021; H. Wang & Huang, 2020; Yolsal-Çevikbilen et al., 2012; Zhao et al., 2010). Accordingly, we found that the locations of the 20 February 2023 *Mw* 6.4 and *Mw* 5.2 earthquakes are adjacent to the distinct separation zone between the low and moderately high Vp anomalies at 12 km depth in the tomographic images of H. Wang et al. (2020). Similarly, some of the relatively deep aftershocks (>20 km D-D′, F-F′, G-G′) shown in the cross-sections could be correlated with this Vp transition, which is evident at depths between 4 and 21 km along the Amanos segment of the EAFZ. The identification of a close correlation between the co-seismic slip evolution on a fault zone and the complex features of the crustal structures beneath the regions can be a remarkable signature for estimating the possible locations of future earthquakes.

Furthermore, our results confirm the transtensional deformation associated with the left-lateral strike-slip fault segments with a significant dip-slip component in the Hatay-Syria region. This deformation pattern plays an important role in the earthquake generation process and the geodynamic evolution of the region. The dominant motion in this area could also be inferred from the analysis of earthquake slip vectors and tensional (T) and compressional (P) axis directions. Here, we calculated the T-axis directions from the focal mechanism solutions of earthquakes in the study region (Table 1), and found that they apparently confirmed the ongoing NE-SW and E-W oriented extensional deformation, as suggested by Över et al. (2002).

5.2. Implications From the GNSS Data Modeling

Near the epicenter of the 20 February 2023 *Mw* 6.4 Hatay earthquake, statistically significant displacements in the southwest direction were observed at the nearby stations, while at the far-field stations, except for the station ANTE, no significant displacements were observed. The SW oriented displacements quantified at near-field stations confirm the left-lateral strike-slip character of the SAFZ. Due to the heterogeneous distribution of stations near the epicenter of the earthquake and the fact that these stations are mainly located at the west of the strike-slip fault, the magnitudes of the displacements in the northeast direction could not be determined with this approach. Nevertheless, the lateral variation of vector orientations observed at far-field stations implies a consistent displacement direction within this region. Considering that the uncertainties in displacement estimates obtained from GNSS data are below centimeters, increasing the point density and homogenizing the station distribution in fault zones will enable better constrained fault models and help us in revealing the regional effects of earthquake-induced displacements (Figure 9).

6. Conclusion

The complex interaction between the Arabian, the African, and Anatolian plates is responsible for the development of major tectonic structures (e.g., EAFZ, DSFZ, SAFZ) in SE Türkiye. After the 2023 destructive earthquakes, stress accumulation on different segments of the EAFZ and re-activation of several faults with intense seismicity have been observed in this tectonically complex area. The epicenters of the 2023 Hatay earthquakes are close to the triple junction area in southern Türkiye, where the EAFZ, DSFZ and the Cyprus Arc merge. In the present study, the type of deformation patterns in the region, the source characteristics and rupture kinematics of the 20 February 2023 *Mw6.4* Hatay (southern Türkiye) earthquake were estimated by analyzing seismological data recorded at both near-field SGM and far-field weak motion broadband seismic stations, and high-rate GNSS data. The results clearly reveal the transtensional deformation in the Hatay-Syria region, resulting in recent earthquake sequences along the major faults in the southern part of Türkiye (e.g., SAFZ, EAFZ, DSFZ; Figures 1 and 3). The analysis of limited GNSS data at the near-field stations revealed notable south-westerly co-seismic displacements, confirming the oblique slip character of the SAFZ (Figures 9 and 10). In addition to horizontal motions, significant vertical offsets were defined at near-field stations such as HAT2 and ARST, indicating extensional motion in this region (Table S7 in Supporting Information S1).

The distribution of the relocated earthquakes (Figure 3) and the Coulomb stress calculation models reported in previously published studies evidently indicate the earthquake-prone areas along the segments of EAFZ and DSFZ in the future. Furthermore, earlier studies based on historical documents and numerical tsunami simulations indicated noteworthy earthquake-induced tsunami waves along the coasts of Hatay, Syria, and the Levantine basin in the Eastern Mediterranean. However, the 2023 *Mw* 6.4 earthquake did not produce notable tsunami waves in the nearby coastal areas. The relatively small amount of released seismic energy and inadequate size of vertical slip on the fault plane of the 2023 *Mw* 6.4 earthquake might not play critical roles in producing notable tsunami waves at the nearby coasts. Nevertheless, it serves as a reminder of the seismic and tsunami hazard potential in the area. In conclusion, the overall results help us to better understand the potential seismic and tsunami hazard of earthquakes in the Türkiye-Syria region. We emphasize the continued high potential for large earthquakes and associated tsunamis in the Hatay - Syria region due to the stress accumulation at the southern end of the EAFZ and the northern part of the DSFZ following the 2023 SE Türkiye *Mw* 7.8 and *Mw* 7.6 earthquakes.

Data Availability Statement

Strong ground motion seismograms and initial catalogue of aftershocks and phase-arrival data acquired from their bulletin resources for the period 6 February 2023–8 May 2023 were downloaded from the web page of Disaster and Emergency Management Presidency of Türkiye (AFAD-TK, https://tdvms.afad.gov.tr) and BU-KOERI. Teleseismic body waveform data used are from the International Federation of Digital Seismograph Networks (FDSN) and the Global Digital Seismograph Network (GDSN) stations and archived at the IRIS Data Management Centre (IRIS-DMC, http://ds.iris.edu/wilber3). We would also like to thank the General Directorate of Mapping, General directorate of Land Registry and Cadastre, ELYA Technology company and Adana Metropolitan Municipality for providing the GNSS/CORS data used in this study. The Generic Mapping Tools (GMT; Wessel & Smith, 1998) and SAC2000 (Goldstein et al., 2003; Goldstein & Snoke, 2005) software packages were used for the preparation of some of the figures and for processing conventional earthquake data.

Acknowledgments

We would like to thank Istanbul Technical University Research Fund (İTÜ-BAP), the National Scientific and Technological Research Council of Türkiye (TÜBİTAK), Turkish Academy of Sciences (TÜBA) in the framework for Young Scientist Award Program (TÜBA-GEBİP), The Science Academy Chamber—Türkiye (BAGEP), and the Alexander von Humboldt Foundation (Germany) Research Fellowship Award for financial support and for further providing computing facilities and other relevant computational resources through Humboldt-Stiftung Follow-Up Programme. We also appreciate Dr. Yuji Yagi's (Tsukuba, Japan) generous permission to use the kinematic slip inversion code to analyze the rupture history and slip distribution models, and his guidance throughout. We are grateful to the Editor and anonymous reviewers for their thoughtful comments, constructive advice, and suggestions that resulted in considerable improvement of this manuscript.

References

Abercrombie, R. E. (1995). Earthquake source scaling relationships from −1 to 5 M_L using seismograms recorded at 2.5-km depth. *Journal of Geophysical Research*, *100*(B12), 24015–24036. https://doi.org/10.1029/95JB02397

AFAD. (2023a). Retrieved from https://deprem.afad.gov.tr/event-detail/415966

AFAD. (2023b). *Pre-evaluation report on 20 February 2023 Yayladağı (Hatay) Mw 6.4 earthquake*. *Disaster and Emergency Management Presidency of Türkiye* (p. 10). Ministry of Interior, Ankara, Türkiye. Retrieved from https://deprem.afad.gov.tr

Akaike, H. (1980). Likelihood and Bayes procedure. In J. M. Bernardo, M. H. DeGroot, D. V. Lindley, & A. F. M. Smith (Eds.), *Bayesian Statistics* (pp. 143–166). University Press.

Aki, K. (1972). Earthquake mechanism. *Tectonophysics*, *13*(1–4), 423–446. https://doi.org/10.1016/0040-1951(72)90032-7

Aksu, A. E., Hall, J., & Yaltırak, C. (2008). Miocene-recent evolution of Anaximander Mountain and Finike Basin at the junction of Hellenic and Cyprus arcs, eastern Mediterranean. *Marine Geology*, *258*(1–4), 24–47. https://doi.org/10.1016/j.margeo.2008.04.008

Akyüz, H. S., Altunel, E., Karabacak, V., & Yalçıner, C. C. (2006). Historical earthquake activity of the northern part of the Dead Sea Fault Zone, southern Turkey. *Tectonophysics*, *426*(3–4), 281–293. https://doi.org/10.1016/j.tecto.2006.08.005

Ambraseys, N. N. (1989). Temporary seismic quiescence: SE Turkey. *Geophysical Journal International*, *96*(2), 311–331. https://doi.org/10.1111/j.1365-246X.1989.tb04453.x

Ambraseys, N. N., & Barazangi, M. (1989). The 1759 earthquake in the Bekaa Valley: Implications for earthquake hazard assessment in the Eastern Mediterranean region. *Journal of Geophysical Research*, *94*(B4), 4007–4013. https://doi.org/10.1029/JB094iB04p04007

Ambraseys, N. N., & Jackson, J. A. (1998). Faulting associated with historical and recent earthquakes in the eastern Mediterranean region. *Geophysical Journal International*, *133*(2), 390–406. https://doi.org/10.1046/j.1365-246X.1998.00508.x

Ambraseys, N. N., & Melville, C. P. (1995). Historical evidence of faulting in Eastern Anatolia and Northern Syria. *Annales Geofisica*, *38*(3–4), 337–343. https://doi.org/10.4401/ag-4110

Ambraseys, N. N., Melville, C. P., & Adam, R. D. (1994). *The seismicity of Egypt, Arabia and the Red Sea: A historical review*. Cambridge University Press.

Amiran, D. H. K., Arieh, E., & Turcotte, T. (1994). Earthquakes in Israel and adjacent areas: Macroseismic observations since 100 B.C.E. *Israel Exploration Journal*, *44*(3/4), 260–305.

Arpat, E., & Şaroğlu, F. (1972). The East Anatolian Fault system: Thoughts on its development. *Bulletin of the Mineral Research and Exploration*, *78*, 33–39.

Barbot, S., Luo, H., Wang, T., Hamiel, Y., Piatibratova, O., Javed, M. T., et al. (2023). Slip distribution of the February 6, 2023 Mw 7.8 and Mw 7.6, Kahramanmaraş, Turkey earthquake sequence in the East Anatolian Fault Zone. *Seismica*, *2*(3), 502. https://doi.org/10.26443/seismica.v2i3.502

Bath, M. (1965). Lateral inhomogeneities of the upper mantle. *Tectonophysics*, *2*(6), 483–514. https://doi.org/10.1016/0040-1951(65)90003-X

Ben-Avraham, Z., Garfunkel, Z., & Lazar, M. (2008). Geology and evolution of the southern Dead Sea Fault with emphasis on subsurface structure. *Annual Review of Earth and Planetary Sciences*, *36*(1), 357–387. https://doi.org/10.1146/annurev.earth.36.031207.124201

Ben-Menahem, A. (1979). Earthquake catalogue for the Middle East (92 B.C. to 1980 A.D.). *Bollettino di Geofisica Teorica ed Applicata*, *21*, 245–313.

Bozkurt, E. (2001). Neotectonics of Turkey – A synthesis. *Geodinamica Acta*, *14*(1–3), 3–30. https://doi.org/10.1016/S0985-3111(01)01066-X

Çalışkan, C. (2002). *Source parameters solutions of 3 August 1993, 22 November 1995 and 22 January 1997 earthquakes* (M.Sc. Thesis) (p. 139). Istanbul Technical University, Graduate School of Science and Technology. (in Turkish with English Abstract).

Carena, S., Friedrich, A. M., Verdecchia, A., Kahle, B., Rieger, S., & Kübler, S. (2023). Identification of source faults of large earthquakes in the Turkey-Syria border region between 1000 CE and the present, and their relevance for the 2023 Mw 7.8 Pazarcık earthquake. *Tectonics*, *42*(12), e2023TC007890. https://doi.org/10.1029/2023TC007890

Cheng, B., Zhao, D., Cheng, S., Ding, Z., & Zhang, G. (2016). Seismic tomography and anisotropy of the Helan-Liupan tectonic belt: Insight into lower crustal flow and seismotectonics. *Journal of Geophysical Research: Solid Earth*, *121*(4), 2608–2635. https://doi.org/10.1002/2015JB012692

Confal, J. M., Bezada, M. J., Eken, T., Faccenda, M., Saygin, E., & Taymaz, T. (2020). Influence of upper mantle anisotropy on isotropic P-wave tomography images obtained in the Eastern Mediterranean region. *Journal of Geophysical Research: Solid Earth*, *125*(8), e2019JB018559. https://doi.org/10.1029/2019JB018559

Çubuk, Y., Yolsal-Çevikbilen, S., & Taymaz, T. (2014). Source parameters of Bala-Sirapinar (Central Turkey) earthquakes of 2005–2008: Implications on internal deformation of the Anatolian Plate. *Tectonophysics*, *635*, 125–153. https://doi.org/10.1016/j.tecto.2014.07.005

Dai, X., Liu, X., Liu, R., Song, M., Zhu, G., Chang, X., & Guo, J. (2024). Coseismic slip distribution and Coulomb stress change of the 2023 Mw 7.8 Pazarcik and Mw 7.5 Elbistan earthquakes in Turkey. *Remote Sensing*, *16*(2), 240. https://doi.org/10.3390/rs16020240

Dewey, J. F., Hempton, M. R., Kidd, W. S. F., Saroglu, F., & Sengör, A. M. C. (1986). Shortening of continental lithosphere: The neotectonics of Eastern Anatolia – A young collision zone. In M. P. Coward & A. C. Ries (Eds.), *Collision tectonics*, *Geological Society, London, Special Publications* (Vol. 19, pp. 3–36).

Ding, H. Y., Zhou, Y. J., Ge, Z. X., Taymaz, T., Ghosh, A., Xu, H. Y., et al. (2023). High-resolution seismicity imaging and early aftershock migration of the 2023 Kahramanmaraş (SE Türkiye) M_W 7.9 & 7.8 earthquake doublet. *Earthquake Science*, *36*(6), 417–432. https://doi.org/10.1016/j.eqs.2023.06.002

Dogan, A. H., Tunalioglu, N., Erdogan, B., & Ocalan, T. (2018). Evaluation of the GPS Precise Point Positioning technique during the 21 July 2017 Kos-Bodrum (East Aegean Sea) Mw 6.6 earthquake. *Arabian Journal of Geosciences*, *11*(24), 775. https://doi.org/10.1007/s12517-018-4140-z

Dreger, D., Ritsema, J., & Pasyanos, M. (1995). Broadband analysis of the 21 September, 1993 Klamath Falls earthquake sequence. *Geophysical Research Letters*, *22*(8), 997–1000. https://doi.org/10.1029/95GL00566

Dreger, D. S. (2003). TDMT_INV: Time domain seismic moment tensor INVersion. In W. K. Lee (Ed.), *International Handbook of Earthquake and Engineering Seismology* (Vol. 81B, p. 1627). Academic Press.

Dreger, D. S., & Helmberger, D. V. (1993). Determination of source parameters at regional distances with single station or sparse network data. *Journal of Geophysical Research*, *98*(B5), 8107–8125. https://doi.org/10.1029/93JB00023

Duman, T. Y., Elmacı, H., Özalp, S., Kürçer, A., Kara, M., Özdemir, E., et al. (2020). Paleoseismology of the western Sürgü–Misis fault system: East Anatolian Fault, Turkey. *Mediterranean Geoscience Reviews*, *2*(3), 411–437. https://doi.org/10.1007/s42990-020-00041-6

Duman, T. Y., & Emre, Ö. (2013). The East Anatolian Fault: Geometry segmentation and jog characteristics. *Geological Society, London, Special Publications*, *372*(1), 495–529. https://doi.org/10.1144/SP372.14

Dziewonski, A. M., & Anderson, D. L. (1981). Preliminary Reference Earth Model (PREM). *Physics of the Earth and Planetary Interiors*, *25*(4), 297–356. https://doi.org/10.1016/0031-9201(81)90046-7

Eken, T. (2019). Moment magnitude estimates for central Anatolian earthquakes using coda waves. *Solid Earth*, *10*(3), 713–723. https://doi.org/10.5194/se-10-713-2019

Emre, Ö., Duman, T. Y., Özalp, S., Elmacı, H., & Olgun, Ş. (2012). *1:250.000 scale active fault map series of Turkey*. General Directorate of Mineral Research and Exploration.

Emre, Ö., Duman, T. Y., Özalp, S., Şaroğlu, F., Olgun, Ş., Elmacı, H., & Çan, T. (2018). Active fault database of Turkey. *Bulletin of Earthquake Engineering*, *16*(8), 3229–3275. https://doi.org/10.1007/s10518-016-0041-2

Emre, Ö., Duman, T. Y., Özalp, S., Elmacı, H., Olgun, Ş., & Şaroğlu, F. (2013). *Active Fault Map of Turkey with an Explanatory Text. 1:1.250.000 Scale, VI+89 pp.+one sheet*. Special Publication Series-30. General Directorate of Mineral Research and Exploration. Retrieved from https://www.mta.gov.tr/en/

Ergin, K., Güçlü, U., & Uz, Z. (1967). *Earthquake catalogue of Turkey and surroundings*. Faculty of Mines Printing House, No: 24, Istanbul Technical University. (in Turkish).

Eulenfeld, T., & Wegler, U. (2016). Measurement of intrinsic and scattering attenuation of shear waves in two sedimentary basins and comparison to crystalline sites in Germany. *Geophysical Journal International*, *205*(2), 744–757. https://doi.org/10.1093/gji/ggw035

Fielding, E. J., Lundgren, P. R., Taymaz, T., Yolsal-Çevikbilen, S., & Owen, S. E. (2013). Fault-slip source models for the 2011 M7.1 Van earthquake in Turkey from SAR interferometry, pixel offset tracking, GPS and seismic waveform analysis. *Seismological Research Letters*, *84*(4), 579–593. https://doi.org/10.1785/0220120164

Freund, R. (1965). A model of the structural development of Israel and adjacent areas since Upper Cretaceous times. *Geological Magazine*, *102*(3), 189–205. https://doi.org/10.1017/s0016756800053218

Fukahata, Y., Yagi, Y., & Matsu'ura, M. (2003). Waveform inversion for seismic source processes using ABIC with two sorts of prior constraints: Comparison between proper and improper formulations. *Geophysical Research Letters*, *30*(6), 1305. https://doi.org/10.1029/2002GL016293

Gardosh, M. A., & Druckman, Y. (2006). Seismic stratigraphy, structure and tectonic evolution of the Levantine Basin, offshore Israel. In A. H. F. Robertson & D. Mountrakis (Eds.), *Tectonic development of the Eastern Mediterranean Region* (Vol. 260, pp. 201–227). Geological Society, London, Special Publications.

Garfunkel, Z., Zak, Y., & Freund, R. (1981). Active faulting in the Dead Sea rift. *Tectonophysics*, *80*(1–4), 1–26. https://doi.org/10.1016/0040-1951(81)90139-6

GFZ. (2023). Retrieved from https://geofon.gfz-potsdam.de/old/data/alerts/2023/gfz2023dhoi/mt.txt

Goldberg, D. E., Taymaz, T., Reitman, N. G., Hatem, A. E., Yolsal-Çevikbilen, S., Barnhart, W. D., et al. (2023). Rapid characterization of the February 2023 Kahramanmaraş, Türkiye, earthquake sequence. *The Seismic Record*, *3*(2), 156–167. https://doi.org/10.1785/0320230009

Goldberg, D. E., Taymaz, T., Yeck, W. L., Barnhart, W. D., Yolsal- Çevikbilen, S., Irmak, T. S., et al. (2023). Supporting data and models for characterizing the February 2023 Kahramanmaraş, Türkiye, earthquake sequence. *U.S. Geological Survey Data Release*. USGS – Science Base. https://doi.org/10.5066/P9R6DSVZ

Goldstein, P., Dodge, D., Firpo, M., Minner, L., Kanamori, H., & Jennings, P. C. (2003). SAC2000: Signal processing and analysis tools for seismologists and engineers. In W. H. K. Lee & C. Kisslinger (Eds.), *Invited Contribution to the IASPEI International Handbook of earthquake and Engineering Seismology*. Academic Press.

Goldstein, P., & Snoke, A. (2005). *SAC Availability for the IRIS Community*. Incorporated Institutions for Seismology Data Management Centre Electronic Newsletter.

Guidoboni, E., Bernardini, F., & Comastri, A. (2004). The 1138–1139 and 1156–1159 destructive seismic crises in Syria, south-eastern Turkey and northern Lebanon. *Journal of Seismology*, *8*(1), 105–127. https://doi.org/10.1023/B:JOSE.0000009502.58351.06

Guidoboni, E., & Comastri, A. (2005). *Catalogue of earthquakes and tsunamis in the Mediterranean area from the 11th to the 15th century* (p. 1037). INGV-SGA.

Gutenberg, B., & Richter, C. F. (1954). *Seismicity of the Earth and associated phenomena* (Vol. 9, p. 310). Princeton University Press.

Güvercin, S. E., Karabulut, H., Konca, A. O., Doğan, U., & Ergintav, S. (2022). Active seismotectonics of the East Anatolian Fault. *Geophysical Journal International*, *230*(1), 50–69. https://doi.org/10.1093/gji/ggac045

Hall, J., Aksu, A. E., Yaltırak, C., & Winsor, J. D. (2008). Structural architecture of the Rhodes Basin: A deep depocentre that evolved since the Pliocene at the junction of Hellenic and Cyprus arcs, eastern Mediterranean. *Marine Geology*, *258*(1–4), 1–23. https://doi.org/10.1016/j.margeo.2008.02.007

Heidarzadeh, M., Gusman, A. R., & Mulia, I. E. (2023). The landslide source of the eastern Mediterranean tsunami on 6 February 2023 following the Mw 7.8 Kahramanmaraş (Türkiye) inland earthquake. *Geoscience Letters*, *10*(1), 50. https://doi.org/10.1186/s40562-023-00304-8

Hempton, M. R., Dewey, J. F., & Saroglu, F. (1981). The East Anatolian transform fault: Along strike variations in geometry and behavior (abstract). *EOS*, 62393.

Hofstetter, R., Klinger, Y., Amrat, A.-Q., Rivera, L., & Dorbath, L. (2007). Stress tensor and focal mechanisms along the Dead Sea fault and related structural elements based on seismological data. *Tectonophysics*, *429*(3–4), 165–181. https://doi.org/10.1016/j.tecto.2006.03.010

Hu, G., Satake, K., Liu, L., & Du, P. (2023). Origins of the tsunami following the 2023 Turkey–Syria earthquake. *Geophysical Research Letters*, *50*(18), e2023GL103997. https://doi.org/10.1029/2023GL103997

Hubert-Ferrari, A., Lamair, L., Hage, S., Schmidt, S., Çagatay, M. N., & Avsar, U. (2020). A 3800 yr paleoseismic record (Lake Hazar sediments, eastern Turkey): Implications for the East Anatolian Fault seismic cycle. *Earth and Planetary Science Letters*, *538*, 116152. https://doi.org/10.1016/j.epsl.2020.116152

Inbal, A., Ziv, A., Lior, I., Nof, R. N., & Eisermann, A. S. (2023). Non-triggering and then triggering of a repeating aftershock sequence in the Dead Sea by the 2023 Kahramanmaraş earthquake pair: Implications for the physics of remote delayed aftershocks. *Geophysical Research Letters*, *50*(18), e2023GL104908. https://doi.org/10.1029/2023GL104908

Irmak, T. S. (2013). Focal mechanisms of small-moderate earthquakes in Denizli Graben (SW Turkey). *Earth, Planets and Space*, *65*(9), 943–955. https://doi.org/10.5047/eps.2013.05.011

Irmak, T. S., Bulut, I., & Doğan, B. (2020). Regional seismicity in Adıyaman-Samsat (SE Turkey). *Bollettino di Geofisica Teorica ed Applicata*, *61*(4), 451–468. https://doi.org/10.4430/bgta0322

Irmak, T. S., Yolsal-Çevikbilen, S., Eken, T., Doğan, B., Erman, C., Yavuz, E., et al. (2021). Source characteristics and seismotectonic implications of the 26 September 2019 Mw 5.7 Silivri High-Kumburgaz Basin earthquake and evaluation of its aftershocks at the North Anatolian Fault Zone (Central Marmara Sea, NW Turkey). *Geophysical Journal International*, *227*(1), 383–402. https://doi.org/10.1093/gji/ggab233

Jackson, J. A., & McKenzie, D. (1984). Active tectonics of the Alpine-Himalayan Belt between western Turkey and Pakistan. *Geophysical Journal of the Royal Astronomical Society*, *77*(1), 185–264. https://doi.org/10.1111/j.1365-246X.1984.tb01931.x

Jeffreys, H., & Bullen, K. E. (1958). *Seismological tables*. Office of the British Association, Burlington House.

Kalafat, D., Gürbüz, C., & Üçer, B. (1987). Batı Türkiye'de kabuk ve üst manto yapısının araştırılması. *Deprem Araştırma Bülteni*, *59*, 43–64. (in Turkish).

Kanamori, H. (1994). Mechanics of earthquakes. *Annual Review of Earth and Planetary Sciences*, *22*(1), 207–237. https://doi.org/10.1146/annurev.ea.22.050194.001231

Kanamori, H., & Anderson, D. L. (1975). Theoretical basis of some empirical relations in seismology. *Bulletin of the Seismological Society of America*, *65*(5), 1073–1095. https://doi.org/10.1785/BSSA0650051073

Karabulut, H., Güvercin, S. E., Hollingsworth, J., & Konca, A. Ö. (2023). Long silence on the East Anatolian Fault Zone (Southern Turkey) ends with devastating double earthquakes (6 February 2023) over a seismic gap: Implications for the seismic potential in the Eastern Mediterranean region. *Geological Society of London*, *180*(3), jgs2023-021. https://doi.org/10.6084/m9.figshare.c.6567094.v2

Kempler, D., & Garfunkel, Z. (1994). Structures and kinematics in the north-eastern Mediterranean: A study of an irregular plate boundary. *Tectonophysics*, *234*(1–2), 19–32. https://doi.org/10.1016/0040-1951(94)90202-X

Khair, K., Karakaisis, G. F., & Papadimitriou, E. E. (2000). Seismic zonation of the Dead Sea Transform Fault area. *Annali di Geofisica*, *43*(1), 61–79. https://doi.org/10.4401/ag-3620

Kikuchi, M., & Kanamori, H. (1991). Inversion of complex body waves – III. *Bulletin of the Seismological Society of America*, *81*(6), 2335–2350. https://doi.org/10.1785/BSSA0810062335

Kissling, E., Ellsworth, W. L., Eberhart-Phillips, D., & Kradolfer, U. (1994). Initial reference models in local earthquake tomography. *Journal of Geophysical Research*, *99*(B10), 19635–19646. https://doi.org/10.1029/93JB03138

Klein, F. W. (2014). *User's Guide to HYPOINVERSE-2000, a Fortran Program to solve for earthquake locations and magnitude*. Open File Report 02-171. U.S. Geological Survey.

KOERI. (2023a). *Earthquake list of February 2023*. Bogazici University, Kandilli Observatory and Earthquake Research Institute – Regional Earthquake Tsunami Monitoring Center. Retrieved from http://udim.koeri.boun.edu.tr/zeqmap/hgmmap.asp#

KOERI. (2023b). *A report on 20 February 2023 Büyükçat-Samandağ-Hatay earthquakes* (p. 5). Bogazici University, Kandilli Observatory and Earthquake Research Institute – Regional Earthquake Tsunami Monitoring Center. Retrieved from http://www.koeri.boun.edu.tr/sismo/2/20-subat-2023-ml6-4-buyukcat-samandag-hatay-depremi/

KOERI-UDIM. (2012). Historical earthquakes. Retrieved from http://www.koeri.boun.edu.tr/sismo/2/deprem-bilgileri/buyuk-depremler/

Larson, K. M., & Miyazaki, S. (2008). Resolving static offsets from high-rate GPS data: The 2003 Tokachi-oki earthquake. *Earth Planet Space*, *60*(8), 801–808. https://doi.org/10.1186/BF03352831

Li, S., Wang, X., Tao, T., Zhu, Y., Qu, X., Li, Z., et al. (2023). Source model of the 2023 Turkey earthquake sequence imaged by Sentinel-1 and GPS measurements: Implications for heterogeneous fault behavior along the East Anatolian Fault Zone. *Remote Sensing*, *15*(10), 2618. https://doi.org/10.3390/rs15102618

Liu, C., Lay, T., Wang, R., Taymaz, T., He, Z., Xiong, X., et al. (2023). Complex multi-fault rupture and triggering during the 2023 earthquake doublet in southeastern Türkiye. *Nature Communications*, *14*(1), 5564. https://doi.org/10.1038/s41467-023-41404-5

Lyberis, N., Yürür, T., Chorowicz, J., Kasapoglu, E., & Gündogdu, N. (1992). The East Anatolian Fault: An oblique collisional belt. *Tectonophysics*, *204*(1–2), 1–15. https://doi.org/10.1016/0040-1951(92)90265-8

Maggi, A., Jackson, J., Priestley, K., & Baker, C. (2000). A re-assessment of focal distributions in southern Iran, the Tien Shan and northern India: Do earthquakes really occur in the continental mantle? *Geophysical Journal International*, *143*(3), 629–661. https://doi.org/10.1046/j.1365-246X.2000.00254.x

Mai, P. M., Aspiotis, T., Aquib, T. A., Cano, E. V., Castro-Cruz, D., Espindola-Carmona, A., et al. (2023). The Destructive earthquake doublet of 6 February 2023 in south-central Türkiye and Northwestern Syria: Initial observations and analyses. *The Seismic Record*, *3*(2), 105–115. https://doi.org/10.1785/0320230007

Martin, A., Anquela, A. B., Dimas-Pagés, A., & Cos-Gayón, F. (2015). Validation of performance of real-time kinematic PPP. A possible tool for deformation monitoring. *Measurement*, *69*, 95–108. https://doi.org/10.1016/j.measurement.2015.03.026

McCaffrey, R., & Abers, G. (1988). *SYN3: A program for inversion teleseismic body waveforms on microcomputers*. Air force Geophysics Laboratory Technical Report (p. 50). AFGI-TR-88-0099, Hanscomb Air Force Base.

McCaffrey, R., & Nábělek, J. L. (1987). Earthquakes, gravity, and the origin of the Bali Basin: An example of a nascent continental fold-and-thrust belt. *Journal of Geophysical Research*, *92*(B1), 441–460. https://doi.org/10.1029/JB092iB01p00441

McCaffrey, R., Zwick, P., & Abers, G. (1991). *SYN4 program* (Vol. 3, pp. 81–166). IASPEI Software Library. https://doi.org/10.1016/S0074-6142(03)80281-4

McClusky, S., Balassanian, S., Barka, A., Demir, E., Ergintav, S., Georgiev, I., et al. (2000). Global Positioning System constraints on plate kinematics and dynamics in the Eastern Mediterranean and Caucasus. *Journal of Geophysical Research*, *105*(B3), 5695–5719. https://doi.org/10.1029/1999JB900351

McKenzie, D. (1976). The East Anatolian Fault: A major structure in Eastern Turkey. *Earth and Planetary Science Letters*, *29*(1), 189–193. https://doi.org/10.1016/0012-821X(76)90038-8

Medvedeva, A., Vydrin, D., Krylov, A., Shiryborova, A., Smirnova, D., Tsukanova, E., et al. (2023). The Turkish Tsunami of 6 February 2023 in the Northeastern Mediterranean. *Pure and Applied Geophysics*, *180*(9), 3177–3193. https://doi.org/10.1007/s00024-023-03341-8

Melgar, D., Ganas, A., Taymaz, T., Valkaniotis, S., Crowell, B., Kapetanidis, V., et al. (2020). Rupture kinematics of January 24, 2020 Mw 6.7 Doğanyol-Sivrice, Turkey earthquake on the East Anatolian Fault Zone imaged by space geodesy. *Geophysical Journal International*, *223*(2), 862–874. https://doi.org/10.1093/gji/ggaa345

Melgar, D., Taymaz, T., Ganas, A., Crowell, B., Öcalan, T., Kahraman, M., et al. (2023). Sub- and super-shear ruptures during the 2023 Mw 7.8 and Mw 7.6 earthquake doublet in SE Türkiye. *Seismica*, *2*(3). https://doi.org/10.26443/seismica.v2i3.387

METU-EERC. (2023). Middle East Technical University Preliminary Reconnaissance Report on February 6, 2023, Pazarcık Mw=7.7 and Elbistan Mw=7.6, Kahramanmaraş-Türkiye Earthquakes. Report No: METU/EERC 2023-01.

MTA. (2023). *Preliminary field and evaluation report on 20 February 2023 Defne - Hatay (Mw 6.4) Earthquake* (p. 4). General Directorate of Mineral Research and Explorations of Turkey (MTA), Ministry of Energy and Natural Resources. Retrieved from https://www.mta.gov.tr/

Nur, A., & Ben-Avraham, Z. (1978). The eastern Mediterranean and the Levant: Tectonics of continental collision. *Tectonophysics*, *46*(3–4), 297–311. https://doi.org/10.1016/0040-1951(78)90209-3

OCA. (2023). Regional focal mechanism solutions reported by SISMOAZUR. Retrieved from https://sismoazur.oca.eu/#/focal_mechanism/emsc/

Ocalan, T., Turk, T., Tunalioglu, N., & Gurturk, M. (2022). Investigation of accuracy of PPP and PPP-AR methods for direct georeferencing in UAV photogrammetry. *Earth Science Informatics*, *15*(4), 2231–2238. https://doi.org/10.1007/s12145-022-00868-7

Okuwaki, R., Yagi, Y., Taymaz, T., & Hicks, S. (2023). Multi-scale rupture growth with alternating directions in a complex fault network during the 2023 south-eastern Türkiye and Syria earthquake doublet. *Geophysical Research Letters*, *50*(12), e2023GL103480. https://doi.org/10.1029/2023GL103480

Omori, F. (1894). *On the aftershocks of earthquakes* (Vol. 7, pp. 111–200). Journal of the College of Science, Imperial University of Tokyo.

Över, S., Demirci, A., & Özden, S. (2023). Tectonic implications of the February 2023 Earthquakes (Mw7.7, 7.6 and 6.3) in south-eastern Türkiye. *Tectonophysics*, *866*, 230058. https://doi.org/10.1016/j.tecto.2023.230058

Över, S., Ünlügenç, U. C., & Bellier, O. (2002). Quaternary stress regime change in the Hatay region, SE Turkey. *Geophysical Journal International*, *148*(3), 649–662. https://doi.org/10.1046/j.1365-246X.2002.01621.x

Pasyanos, M. E., Dreger, D. S., & Romanowicz, B. (1996). Towards real-time determination of regional moment tensors. *Bulletin of the Seismological Society of America*, *86*(5), 1255–1269. https://doi.org/10.1785/BSSA0860051255

Petersen, G. M., Buyukakpinar, P., Sanhueza, F. O. V., Metz, M., Cesca, S., Akbayram, K., et al. (2023). The 2023 Southeast Türkiye seismic sequence: Rupture of a complex fault network. *The Seismic Record*, *3*(2), 134–143. https://doi.org/10.1785/0320230008

Plassard, J., & Kogoj, B. (1981). *Seismicité du Liban: catalogue des seismes ressentis*. *Annales-Mémoires de l'Observatoire de Ksara* (3rd ed., Vol. 4, p. 67). CNRS.

Poirier, J. P., Romanowicz, B. A., & Taher, M. A. (1980). Large historical earthquakes and seismic risk in Northwest Syria. *Nature*, *285*(5762), 217–220. https://doi.org/10.1038/285217a0

Ragon, T., Simons, M., Bletery, Q., Cavalié, O., & Fielding, E. (2021). A stochastic view of the 2020 Elazığ Mw 6.8 earthquake (Turkey). *Geophysical Research Letters*, *48*(3), e2020GL090704. https://doi.org/10.1029/2020GL090704

Reilinger, R., McClusky, S., Vernant, P., Lawrence, S., Ergintav, S., Cakmak, R., et al. (2006). GPS constraints on continental deformation in the Africa-Arabia-Eurasia continental collision zone and implications for the dynamics of plate interactions. *Journal of Geophysical Research*, *111*(B5), B05411. https://doi.org/10.1029/2005JB004051

Saikia, C. K. (1994). Modified frequency-wave number algorithm for regional seismograms using Filon's quadrature: Modelling of L_g waves in eastern North America. *Geophysical Journal International*, *118*(1), 142–158. https://doi.org/10.1111/j.1365-246X.1994.tb04680.x

Salamon, A., Hofstetter, A., Garfunkel, Z., & Ron, H. (1996). Seismicity of the eastern Mediterranean region: Perspective from the Sinai subplate. *Tectonophysics*, *263*(1–4), 293–305. https://doi.org/10.1016/S0040-1951(96)00030-3

Salamon, A., Hofstetter, A., Garfunkel, Z., & Ron, H. (2003). Seismotectonics of the Sinai subplate-the eastern Mediterranean region. *Geophysical Journal International*, *155*(1), 149–173. https://doi.org/10.1046/j.1365-246X.2003.02017.x

Şaroğlu, F., Emre, Ö., & Kuşçu, İ. (1992a). *Active Fault Map of Turkey. 2 sheets*. General Directorate of Mineral Research and Exploration-MTA.

Şaroğlu, F., Emre, Ö., & Kuşçu, İ. (1992b). The East Anatolian Fault Zone of Turkey. Special Issue. *Annales Tectonicae*, *6*, 99–125.

Sbeinati, M. R., Darawcheh, R., & Mouty, M. (2005). The historical earthquakes of Syria: An analysis of large and moderate earthquakes from 1365 B.C. to 1900 A.D. *Annales of Geophysics*, *48*(3), 347–435.

Schattner, U., & Ben-Avraham, Z. (2007). Transform margin of the northern Levant, eastern Mediterranean: From formation to reactivation. *Tectonics*, *26*(5). https://doi.org/10.1029/2007TC002112

Şengör, A. M. C., Gorur, N., & Şaroglu, F. (1985). Strike slip faulting and related basin formation in zones of tectonic escape: Turkey as a case study. In *Strike slip deformation, basin formation, and sedimentation* (Vol. 37, pp. 227–264). Society of Economic Paleontologists and Mineralogists. https://doi.org/10.2110/pec.85.37.0211

Sens-Schönfelder, C., & Wegler, U. (2006). Passive image interferometry and seasonal variations of seismic velocities at Merapi Volcano, Indonesia. *Geophysical Research Letters*, *33*(21), L21302. https://doi.org/10.1029/2006GL027797

Snoke, J. A., Munsey, J. W., Teague, A. C., & Bollinger, G. A. (1984). A program for focal mechanism determination by combined use of polarity and SV-P amplitude ratio data. *Earthquake Notes*, *55*(3), 15.

Soloviev, S. L., Solovieva, O. N., Go, C. N., Kim, K. S., & Shchetnikov, N. A. (2000). Tsunamis in the Mediterranean Sea 2000 B.C.–2000 A.D. In *Advances in natural and technological hazards Research* (Vol. 13). Kluwer. https://doi.org/10.1007/978-94-015-9510-0

Stein, R. S., Toda, S., Özbakir, A. D., Sevilgen, V., Gonzalez-Huizar, H., Lotto, G., & Sevilgen, S. (2023). *Interactions, stress changes, mysteries, and partial forecasts of the 2023 Kahramanmaraş, Türkiye, earthquakes*. Temblor. https://doi.org/10.32858/temblor.299

Tan, O. (2004). *The source mechanism properties and rupture histories of the Caucasian, Eastern Anatolian and North Western Iranian Earthquakes*. Ph.D. Thesis (p. 308). Graduate School of Institute of Science and Technology, İstanbul Technical University. (in Turkish with English abstract).

Tan, O., & Taymaz, T. (2006). Active tectonics of the Caucasus: Earthquake source mechanisms and rupture histories obtained from inversion of teleseismic body waveforms. In *Post-collisional tectonics and magmatism in the Mediterranean region and Asia*. *Geological Society of America Special Papers* (Vol. 409, pp. 531–578). https://doi.org/10.1130/2006.2409

Tarı, U., Tüysüz, O., Genç, Ş. C., İmren, C., Blackwell, B. A. B., Lom, N., et al. (2014). The geology and morphology of the Antakya Graben between the Amik Triple Junction and the Cyprus Arc. *Geodinamica Acta*, *26*(1–2), 27–55. https://doi.org/10.1080/09853111.2013.858962

Taymaz, T., Eyidogan, H., & Jackson, J. A. (1991). Source parameters of large earthquakes in the East Anatolian Fault Zone (Turkey). *Geophysical Journal International*, *106*(3), 537–550. https://doi.org/10.1111/j.1365-246X.1991.tb06328.x

Taymaz, T., Ganas, A., Berberian, M., Eken, T., Irmak, T. S., Kapetanidis, V., et al. (2022). The 23 February 2020 Qotur-Ravian earthquake doublet at the Iranian-Turkish border: Seismological and InSAR evidence for escape tectonics. *Tectonophysics*, *838*, 229482. https://doi.org/10.1016/j.tecto.2022.229482

Taymaz, T., Ganas, A., Yolsal-Çevikbilen, S., Vera, F., Eken, T., Erman, C., et al. (2021). Source mechanism and rupture process of the 24 January 2020 *Mw* 6.7 Doğanyol-Sivrice earthquake obtained from seismological waveform analysis and space geodetic observations on the East Anatolian Fault Zone (Turkey). *Tectonophysics*, *804*, 228745. https://doi.org/10.1016/j.tecto.2021.228745

Taymaz, T., Yolsal-Çevikbilen, S., Irmak, T. S., Vera, F., Liu, C., Eken, T., et al. (2022). Kinematics of the 30 October 2020 *Mw* 7.0 Néon Karlovásion (Samos) earthquake in the Eastern Aegean Sea: Implications on source characteristics and dynamic rupture simulations. *Tectonophysics*, *826*, 229223. https://doi.org/10.1016/j.tecto.2022.229223

Templeton, D. C., & Dreger, D. S. (2006). Non-double-couple earthquakes in the long valley volcanic region. *Bulletin of the Seismological Society of America*, *96*(1), 69–79. https://doi.org/10.1785/0120040206

Teunissen, P. J. G. (2021). GNSS precise point positioning. In Y. Morton, F. vanDiggelen, J. Spilker, B. Parkinson, S. Lo, & G. Gao (Eds.), *Position, navigation, and timing technologies in the 21st century: Integrated satellite navigation, sensor systems, and civil applications* (pp. 503–528). Wiley.

Toda, S., Stein, R. S., Özbakir, A. D., Gonzalez-Huizar, H., Sevilgen, V., Lotto, G., & Sevilgen, S. (2023). *Stress change calculations provide clues to aftershocks in 2023 Türkiye earthquakes*. Temblor. https://doi.org/10.32858/temblor.295

Tozer, B., Sandwell, D. T., Smith, W. H. F., Olson, C., Beale, J. R., & Wessel, P. (2019). Global bathymetry and topography at 15 arc sec: SRTM15+. *Earth and Space Science*, *6*(10), 1847–1864. https://doi.org/10.1029/2019EA000658

Türkelli, N., Sandvol, E., Zor, E., Gok, R., Bekler, T., Al-Lazki, A., et al. (2003). Seismogenic zones in eastern Turkey. *Geophysical Research Letters*, *30*(24), 8039. https://doi.org/10.1029/2003GL018023

USGS. (2023a). Retrieved from https://earthquake.usgs.gov/earthquakes/eventpage/us6000jllz/executive

USGS. (2023b). Retrieved from https://earthquake.usgs.gov/earthquakes/eventpage/us6000jlqa/executive

USGS. (2023c). Retrieved from https://earthquake.usgs.gov/earthquakes/eventpage/us6000jqcn/executive

USGS. (2023d). Retrieved from https://earthquake.usgs.gov/earthquakes/eventpage/us6000jqjc/executive

Utsu, T. (1961). A statistical study of the occurrence of aftershocks. *Geophysical Magazine*, *30*, 521–605.

Vanacore, E. A., Taymaz, T., & Saygin, E. (2013). Moho structure of the Anatolian Plate from receiver function analysis. *Geophical Journal International*, *193*(1), 329–337. https://doi.org/10.1093/gji/ggs107

Waldhauser, F., & Ellsworth, W. L. (2000). A double-difference earthquake location algorithm: Method and application to the Northern Hayward Fault, California. *Bulletin of the Seismological Society of America*, *90*(6), 1353–1368. https://doi.org/10.1785/0120000006

Wang, H., & Huang, Z. (2020). Seismic tomography in the southern margin of the Sichuan Basin: Insight into the plateau-craton interaction and seismotectonics in the SE Tibetan plateau. *Journal of Asian Earth Sciences*, *199*, 104464. https://doi.org/10.1016/j.jseaes.2020.104464

Wang, H., Huang, Z., Eken, E., Keleş, D., Kaya-Eken, T., Confal, J. M., et al. (2020). Isotropic and anisotropic P-wave velocity structures of the crust and uppermost mantle beneath Turkey. *Journal of Geophysical Research: Solid Earth*, *125*(12), e2020JB019566. https://doi.org/10.1029/2020JB019566

Wang, Z., Zhang, W., Taymaz, T., He, Z., Xu, T., & Zhang, Z. (2023). Dynamic rupture process of the 2023 Mw 7.8 Kahramanmaraş Earthquake (SE Türkiye): Variable rupture speed and implications for seismic hazard. *Geophysical Research Letters*, *50*(15), e2023GL104787. https://doi.org/10.1029/2023GL104787

Wessel, P., & Smith, W. H. F. (1998). New, improved version of the Generic Mapping Tools released. *Eos, Transactions, American Geophysical Union*, *79*(47), 579. https://doi.org/10.1029/98eo00426

Woodside, J. M., Mascle, J., Zitter, T. A. C., Limonov, A. F., Ergun, M., Volkonskaia, A., & Shipboard Scientists of the PRISMED II Expedition. (2002). The Florence Rise, the western bend of the Cyprus Arc. *Marine Geology*, *185*(3–4), 177–194. https://doi.org/10.1016/S0025-3227(02)00194-9

Wu, F., Xie, J., An, Z., Lyu, C., Taymaz, T., Irmak, T. S., et al. (2023). Pulse-like ground motion observed during the 6 February 2023 Mw7.8 Pazarcık Earthquake (Kahramanmaraş, SE Türkiye). *Earthquake Science*, *36*(4), 328–339. https://doi.org/10.1016/j.eqs.2023.05.005

Xu, C., Zhang, Y., Hua, S., Zhang, X., Xu, L., Chen, Y., & Taymaz, T. (2023). Rapid source inversions of the 2023 SE Türkiye earthquakes with teleseismic and strong-motion data. *Earthquake Science*, *36*(4), 316–327. https://doi.org/10.1016/j.eqs.2023.05.004

Xu, P., Shi, C., Fang, R., Liu, J., Niu, X., Zhang, Q., & Yanagidani, T. (2013). High-rate precise point positioning (PPP) to measure seismic wave motions: An experimental comparison of GPS PPP with inertial measurement units. *Journal of Geodynamics*, *87*(4), 361–372. https://doi.org/10.1007/s00190-012-0606-z

Yagi, Y., & Fukahata, Y. (2011). Introduction of uncertainty of Green's function into waveform inversion for seismic source processes. *Geophysical Journal International*, *186*(2), 711–720. https://doi.org/10.1111/j.1365-246X.2011.05043.x

Yagi, Y., & Kikuchi, M. (2000). Source rupture process of the Kocaeli, Turkey, earthquake of August 17, 1999, obtained by joint inversion of near-field data and teleseismic data. *Geophysical Research Letters*, *27*(13), 1969–1972. https://doi.org/10.1029/1999GL011208

Yagi, Y., Mikumo, T., & Pacheo, J. (2004). Source rupture process of the Tecoman, Colima, Mexico earthquake of January 22, 2003, determined by joint inversion of teleseismic body wave and near-field data. *Bulletin of the Seismological Society of America*, *94*(5), 1795–1807. https://doi.org/10.1785/012003095

Yagi, Y., Nishimura, N., & Kasahara, A. (2012). Source process of the 12 May 2008 Wenchuan, China, earthquake determined by waveform inversion of teleseismic body waves with a data covariance matrix. *Earth, Planets and Space*, *64*(7), E13–E16. https://doi.org/10.5047/eps.2012.05.006

Yagi, Y., Okuwaki, R., Enescu, B., Hirano, S., Yamagami, Y., Endo, S., & Komoro, T. (2014). Rupture process of the 2014 Iquique Chile Earthquake in relation with the foreshock activity. *Geophysical Research Letters*, *41*(12), 4201–4206. https://doi.org/10.1002/2014GL060274

Yıldız, S. S., Ozkan, A., Yavasoglu, H. H., Masson, F., Tiryakioglu, İ., Alkan, M. N., & Bilgi, S. (2020). Determination of recent tectonic deformations in the vicinity of Adana-Osmaniye-Hatay-Gaziantep triple junction region by half-space modelling. *Comptes Rendus, Géoscience-Sciences de la Planѐte*, *352*(3), 225–234. https://doi.org/10.5802/crgeos.39

Yolsal, S. (2008). *Source mechanism parameters and slip distributions of Crete-Cyprus Arcs, Dead Sea transform fault earthquakes and historical tsunami simulations* (Ph.D. Thesis) (p. 523). Graduate School of Institute of Science and Technology, İstanbul Technical University. (in Turkish with English abstract).

Yolsal, S., Taymaz, T., & Yalçıner, A. C. (2007). Understanding tsunamis, potential source regions and tsunami prone mechanisms in the Eastern Mediterranean. In T. Taymaz, Y. Yılmaz, & Y. Dilek (Eds.), *The Geodynamics of the Aegean and Anatolia*, *Geological Society, London, Special Publications* (Vol. 291, pp. 201–230). https://doi.org/10.1144/sp291.10

Yolsal-Çevikbilen, S., Biryol, C. B., Beck, S., Zandt, G., Taymaz, T., Adıyaman, H. E., & Ozacar, A. A. (2012). 3-D Crustal structure along the North Anatolian Fault Zone in north-central Anatolia revealed by local earthquake tomography. *Geophysical Journal International*, *188*(3), 819–849. https://doi.org/10.1111/j.1365-246X.2011.05313.x

Yolsal-Çevikbilen, S., & Taymaz, T. (2012). Earthquake source parameters along the Hellenic subduction zone and numerical simulations of historical tsunamis in the Eastern Mediterranean. *Tectonophysics*, *536–537*, 61–100. https://doi.org/10.1016/j.tecto.2012.02.019

Yolsal-Çevikbilen, S., & Taymaz, T. (2019). Source characteristics of the 28 September 2018 Mw7.5 Palu-Sulawesi, Indonesia (SE Asia) earthquake based on inversion of teleseismic body waves. *Pure and Applied Geophysics*, *176*(10), 4111–4126. https://doi.org/10.1007/s00024-019-02294-1

Yoshida, S. (1992). Waveform inversion for rupture process using a non-flat seafloor model: Application to 1986 Andreanof Islands and 1985 Chile earthquakes. *Tectonophysics*, *211*(1–4), 45–59. https://doi.org/10.1016/0040-1951(92)90050-G

Yoshida, S., Kokhetsu, K., Shibazaki, B., Sagiya, T., Kato, T., & Yoshida, Y. (1996). Joint inversion of near- and far-field waveforms and geodetic data for rupture process of the 1995 Kobe earthquake. *Journal of Physics of the Earth*, *44*(5), 437–454. https://doi.org/10.4294/jpe1952.44.437

Zahradnik, J., Turhan, F., Efthimios, S., & František, G. (2023). Asperity-like (segmented) structure of the 6 February 2023 Turkish earthquakes. *Earth Ar-Xiv*. https://doi.org/10.31223/X5T666

Zanchi, A., Crosta, G. B., & Darkal, A. N. (2002). Paleostress analyses in NW Syria: Constraints on the Cenozoic evolution of the northwestern margin of the Arabian plate. *Tectonophysics*, *357*(1–4), 255–278. https://doi.org/10.1016/S0040-1951(02)00371-2

Zhang, Y., Tang, X., Liu, D., Taymaz, T., Eken, T., Guo, R., et al. (2023). Geometric controls on cascading rupture of the 2023 Kahramanmaraş earthquake doublet. *Nature Geoscience*, *16*(11), 1054–1060. https://doi.org/10.1038/s41561-023-01283-3

Zhao, D., Santosh, M., & Yamada, A. (2010). Dissecting large earthquakes in Japan: Role of arc magma and fluids. *Island Arc*, *19*(1), 4–16. https://doi.org/10.1111/j.1440-1738.2009.00694.x

Zor, E., Sandvol, E., Gürbüz, C., Türkelli, N., Seber, D., & Barazangi, M. (2003). The crustal structure of the East Anatolian plateau (Turkey) from receiver functions. *Geophysical Research Letters*, *30*(24), 8044. https://doi.org/10.1029/2003GL018192

Zumberge, J. F., Heflin, M. B., Jefferson, D. C., Watkins, M. M., & Webb, F. H. (1997). Precise point positioning for the efficient and robust analysis of GPS data from large networks. *Journal of Geophysical Research*, *102*(B3), 5005–5017. https://doi.org/10.1029/96JB03860

Zwick, P., McCaffrey, R., & Abers, G. (1994). *MT5 program* (Vol. 4). IASPEI Software Library.

References From the Supporting Information

GEBCO-BODC. (1997). *General bathymetric chart of the oceans, digital version*. Distributed on CD-ROM by the British Oceanographic Data Centre.

Kennett, B. L. N., & Engdahl, E. R. (1991). Travel times for global earthquake location and phase association. *Geophysical Journal International*, *105*(2), 429–465. https://doi.org/10.1111/j.1365-246X.1991.tb06724.x

Mai, P. M., & Beroza, G. C. (2000). Source scaling properties from finite-fault-rupture models. *Bulletin of the Seismological Society of America*, *90*(3), 604–615. https://doi.org/10.1785/0119990126

10.1029/2023GC011353

Poirier, J. P., & Taher, M. A. (1980). Historical seismicity in the near and Middle East, North Africa, and Spain from Arabic documents (VII–XVIIIth century). *Bulletin of the Seismological Society of America*, *70*(6), 2185–2201. https://doi.org/10.1785/BSSA0700062185

Scherbaum, F. (1994). *Basic concepts in digital signal processing for seismologists*. Springer-Verlag New York, Inc.

Wells, D. L., & Coppersmith, K. J. (1994). New empirical relationships among magnitude, rupture length, rupture width, rupture area, and surface displacement. *Bulletin of the Seismological Society of America*, *84*(4), 974–1002. https://doi.org/10.1785/BSSA0840040974